The Pennsylvania State University

The Graduate School

College of Earth and Mineral Sciences

LABORATORY, FIELD, AND MODELING ANALYSIS OF SOLUTE TRANSPORT

BEHAVIOR AT THE SHALE HILLS CRITICAL ZONE OBSERVATORY

A Thesis in
Geosciences
by

Brad W. Kuntz

Submitted in Partial Fulfillment
of the Requirements
for the Degree of
Master of Science

December 2010

The thesis of Brad W. Kuntz was reviewed and approved[*] by the following:

Kamini Singha
Assistant Professor of Geosciences
Thesis Advisor

Susan L. Brantley
Professor of Geosciences

Michael N. Gooseff
Assistant Professor of Civil and Environmental Engineering

Richard R. Parizek
Professor of Geology and Geo-Environmental Engineering

Chris J. Marone
Professor of Geosciences
Associate Department Head for the Graduate Program and Research

[*]Signatures are on file in the Graduate School

ABSTRACT

We collected and analyzed breakthrough curve (BTC) data to identify the parameters controlling transport from a series of undisturbed fully saturated soil cores and a field test at the Shale Hills Critical Zone Observatory in central Pennsylvania. The soil cores were collected in a continuous hole extending across the soil profile vertically at one location to quantify how solute transport behavior changes with physical and chemical weathering. Additionally, we performed a field scale doublet tracer test to determine transport behavior within the weathered shale bedrock. Hydraulic conductivity and porosity are as low as 10^{-15} m/s and 0.035, respectively, in the shale bedrock and range as high as 10^{-5} m/s and 0.45, respectively, in the shallow soils. Bromide BTCs demonstrated significant anomalous tailing in soil cores and shale bedrock, which do not fit classical advection-dispersion model equations. To quantify the behavior, numerical simulation of solute transport was carried out with both a mobile-immobile (MIM) model and a continuous-time random walk (CTRW) approach. 1-D MIM modeling results on the soil cores yielded low mass transfer rates (<1/d) coupled with large immobile domains ($\theta_{im}/\theta_{m} \simeq 1.5 - 2$) and revealed that solutes were transported within only 30-40% of the total pore space. MIM modeling results also suggested that immobile porosity is a combination of soil texture, fracture spacing, and porosity development on shale fragments. Similarly, the field scale doublet tracer test between boreholes indicated fractures are controlling transport and the surrounding shale matrix has a large potential to store and retard solute movement. 1-D CTRW results yielded a parameter set indicative of a transport regime that is consistently non-Fickian across the vertical length of the soil profile, identified solute tracer velocities are up to 50 times greater than the average fluid velocity, predicted that anomalous transport behavior could extend for significant periods of time, and identified the need to incorporate a continuum of mass

transfer rates to accurately predict and describe the observed tailing behavior. These modeling results confirmed the important role of preferential flow paths, fractures, and mass transfer between more- and less-mobile fluid domains, and established the need to incorporate a mass transfer process that utilizes a distribution of mass transfer rates.

TABLE OF CONTENTS

LIST OF TABLES

LIST OF FIGURES

ACKNOWLEDGMENTS

Completing this thesis has been a little like trying to catch a greased pig, just when you think you got a handle on it- it starts to get away from you. If it wasn't for the continual adjustments, insights, and enthusiastic encouragement of Kamini Singha, this work would not have excelled. Similarly, the particularly guiding discussions with Mike Gooseff, Susan Brantley, and Lixin Jin have helped to shape my research goals and refine my analysis of solute transport behavior at the Shale Hills Critical Zone Observatory.

Most importantly, I express my gratitude for the undying commitment, support, and encouragement of my sweet wife, Becky. The numerous sacrifices Becky and my children have made to support me these many long years through my educational pursuits are beautiful, and defines the glue that will keep our family united in love forever.

PREFACE

The majority of all life and certainly the human race are supported by the thin-skinned region of the earth's exterior extending from the vegetation canopy down into the shallow subsurface. This delicate region of the earth's exterior, called "the critical zone" by some scientists (Amundson et al., 2007), contains the necessary combination of water, nutrients, vegetation, and mineralogy supporting the existence and continuation of life as we presently know it. Evaluating the many diverse physical, chemical, and bio-geochemical processes that contribute to the creation of and stabilization of the critical zone will promote identification of specific factors helping to maintain this delicate and dynamic region of the earth's exterior.

The rocks beneath our feet are composed of various mineral assemblages contributing to soil formation and potentially regulating the creation of the important components of the critical zone. Weathering, the transformation of rocks and minerals by chemical and physical processes over the course of millennia dictates the development of the soil profile. The process of weathering affects both the physical structure of the soil and chemical composition of the soil. For example, the common mineral plagioclase, whose chemical formula is $NaAlSi_3O_8$, may undergo a transformation or reaction such as

$$2NaAlSi_3O_{8 \text{ Na-Plagioclase}} + 2H_2CO_3 + 9H_2O \rightarrow Al_2Si_2O_5(OH)_{4 \text{ Kaolinite}} + 2Na^+ + 2HCO_3^- + 4H_4SiO_4,$$

where $H_2CO_{3(aq)}$, $9H_2O$ are reacting with plagioclase to produce another mineral kaolinite and other species that are dissolved into the water, Na^+, HCO_3^-, and H_4SiO_4. Notice that with this transformation of plagioclase to kaolinite, the diversity of the elemental composition is simplified and some elements or solutes (e.g. Na^+) are released from the mineral structure into

the pore fluid. Additionally, the above reaction indicates that the loss of these solutes from plagioclase is largely regulated by the availability of water and the presence of H_2CO_3.

The goal of this research is to understand the processes controlling water movement and the transport of solutes through the soils and bedrock at the Shale Hills Critical Zone Observatory (SH-CZO). Water moves through the pore space of geologic media around grain boundaries and/or within features such as fractures or preferential pathways. Identifying the composition, structure, and size of the pathways through which the water and solutes travel enhances our ability to predict the residence time and distribution of solutes within the soil and bedrock. Estimating these properties are important for accurate prediction of solute transport behavior. The Rose Hill Shale bedrock at the SH-CZO is comprised largely of silt- and clay-sized particles (<63 µm). These small particles tend to limit water movement and retard solute transport in the soil and shale bedrock. By performing experiments designed to move solutes through the soil and bedrock we can investigate how physical properties control the residence time of solutes in the critical zone.

Tracer tests are experiments in which we inject a known amount of solute at one point and measure the concentration response at another point over time. This concentration data through time is known as a breakthrough curve (BTC). Comparing mathematical modeling results with the measured BTCs allows us to estimate the available pore space, the average solute velocity, and the retardation of the solute caused by the geologic media. One classical mathematical model is the advective-dispersive equation (ADE), which predicts a nearly symmetric distribution of concentration with respect to time. However, we regularly observe BTCs that are highly asymmetric (Adams and Gelhar, 1992; Silliman and Simpson, 1987; Huang et al., 1995), having earlier-than-predicted arrival of solute and higher concentrations during late

times known as tailing. One way to accommodate for the observed asymmetric behavior is to incorporate the physics that will both accelerate the movement of solutes in early times and retard the transport of solutes during late times. To accommodate early and late behavior observations, some have conceptualized the geologic media as having two distinct fluid regions or domains; one domain wherein the solutes move with the fluid, and one domain wherein the solutes become partially trapped or retarded for a time period. The mobile fluid domain is coupled to the trapping or immobile domain via a mass transfer rate which moves mass between each domain over time regulated by the concentration difference between the regions. During early time the concentration of the mobile domain is high relative to the immobile domain and mass accumulates in the immobile pore space. During late times the concentration of the immobile domain is high relative to the mobile domain and mass returns back to the mobile domain. By incorporating this concept of mass transfer into numerical models, many have been able to successfully match BTCs that exhibit both early breakthrough and long tailing (e.g., Maraqa et al., 1997; Gao et al., 2009). In this work we employ such a solute transport model, which accommodates the physics of mass transfer and permits an estimate of the sizes of the immobile and mobile domains. In collaboration with colleagues from the Weizmann Institute of Science, in Israel, we also explore a more complicated model known as a continuous-time random walk (CTRW) that does not explicitly break the subsurface into two domains, but describes the residence time of solutes as a probability density function.

We collected samples vertically across the soil profile to perform experiments in the laboratory and also carried out an experiment at the field scale to quantify how transport behavior changes as a function of soil depth and material properties, estimate the distribution of the pore space between the mobile and immobile domain, and investigate the timescale of mass

transfer between the two domains with the goal of relating the physical properties of the geologic media to solute transport behavior. We also use CTRW to quantify how "anomalous" the solute behavior is. To complement the tracer experiment data we collect measurements on the hydraulic properties of the soil and bedrock providing some additional restrictions on the mathematical modeling results.

We find that the ability of the soil to transmit fluids and the pore space in which solutes are transmitted decreases with increasing depth into the soil profile. The matrix of the shale bedrock has low permeability and the majority of the pores are less a 1 µm; therefore much of the transport occurs in the fractures of the bedrock. Anomalous solute transport behavior and mass transfer between more- and less-mobile domains is apparent in all of the geologic media measured. In some sections of the soil and within the shale bedrock we find that the mass transfer rate between the domains is slow and the size of the immobile domain is large. This combination of slow mass transfer rates and large immobile domains increases the residence time of solutes in the soil and shale bedrock longer than is predicted by advection and dispersion alone; this has important implications for calculating soil weathering rates, determining the age of groundwater in the catchment, and understanding the distribution of solutes throughout the soil profile and shale bedrock. By accounting for solute retention in immobile pore space and mass transfer between the mobile and immobile domains we can better evaluate the physical and chemical processes controlling the transport of solutes in the soil and bedrock at the SH-CZO.

INTRODUCTION

The Shale Hills Critical Zone Observatory (SH-CZO) has been developed as a natural laboratory to predict the creation and function of regolith within a multidisciplinary context. The flow of water and transport of solutes within this catchment are key to dating groundwater, estimating soil weathering rates, predicting nutrient availability, classifying primary and secondary fluid pathways, and identifying controls on the residence time of solutes in the subsurface (Amundson et al., 2007; Brantley et al., 2007; Anderson et al., 2008; Dere et al., 2010). Identifying groundwater age is a useful means to investigate watershed scale processes including discharge and recharge areas, preferential flow paths, and drought vulnerability or resource protection (Kazemi et al., 2008). Calculating groundwater ages has traditionally been accomplished by advection-only models (e.g., Reilly et al., 1994), although the importance of dispersion and diffusion processes is well recognized (e.g., Goode, 1996; Varni and Carrera, 1998; Bethke and Johnson, 2008). Recent models, such as those described in Duffy (2009), incorporate the diffusion of solutes between dead-end pore space and the advective fluid domain; however, data are required to 1) constrain the residence times of fluids within these more- and less-mobile domains and 2) evaluate the distribution of the pore space within the subsurface. Here, we provide data for these two requirements and explore the assumptions within conceptual transport models at the SH-CZO.

Classically, transport is described by the advection-dispersion equation (ADE). With the ADE, the shape of the breakthrough history is fitted by estimating the dispersivity (e.g., Koch and Fulher, 1993; Perfect et al., 2002; Javaux and Vanclooster, 2003; Vanderborght and Vereecken, 2007). However, the assumption of Fickian transport intrinsic in the ADE prevents its ability to effectively predict and characterize solute transport behavior in heterogeneous

environments (e.g., Adams and Gelhar, 1992; Silliman and Simpson, 1987; Huang et al., 1995; Javaux and Vanclooster, 2004; Gorelick et al., 2005).

Of particular interest in this work is an evaluation of the physical processes trapping solutes in immobile pore space, the matrix, or less-mobile pathways. The SH-CZO's regolith and bedrock are dominated largely by silty-loam soils and fractured shale bedrock that are likely to contain significant immobile pore space (Lin, 2006). Presence of immobile pore space has been documented in many geologic materials and scales ranging from well-sorted sandstone (e.g., Coats and Smith, 1964) to saprolitic soils (e.g., Gwo et al., 2007) and fractured bedrock (e.g., Jardine et al. 1999). Fundamental to quantifying transport within these materials is a sufficient accounting of scale-dependent processes including dispersion, diffusion and mass transfer. Incorporating the transfer of mass between less-mobile pore space and the mobile pore space has facilitated improved fitting of breakthrough curves (BTCs) in many settings where long concentration tailing behavior is seen (e.g., Maraqa et al., 1997; Gao et al., 2009). We follow the approach of Gao et al. (2009) to compare alternative conceptual and numerical models to constrain, predict, and interpret solute transport behavior. Here, we inspect the well-characterized SH-CZO catchment by performing tracer experiments in the laboratory and field to interpret solute transport behavior given two different conceptual transport models of varying complexity. Such an approach identifies where interpretations and a certain parameter space do not consistently meet, and explores the assumptions within the models. Within this framework we 1) characterize the operation of parameters controlling solute transport and groundwater flow at the SH-CZO and 2) converge on an accurate depiction of the subsurface transport behavior by examining the data from different perspectives and modeling techniques.

CONCEPTUAL MODELS OF SOLUTE TRANSPORT

Recognition that heterogeneous environments contain fast and slow paths (e.g., fracture and matrix, mobile and immobile zones, or preferential pathways and dead-end pore space) led to the development of alternative transport models. One simple model is the mobile-immobile (MIM) model (van Genuchten and Wierenga, 1976), shown here in 1-D:

$$\theta_m \frac{\partial c_m}{\partial t} + \theta_{im} \frac{\partial c_{im}}{\partial t} = \theta_m D \frac{\partial^2 c_m}{\partial x^2} - v\theta_m \frac{\partial c_m}{\partial x} \tag{1}$$

where θ is the porosity $\left[cm^3 cm^{-3} \right]$, c is the concentration of the solute $\left[ML^{-3} \right]$, v is the average fluid flow velocity $\left[LT^{-1} \right]$, D is the hydrodynamic dispersion coefficient $\left[L^2 T^{-1} \right]$, and the subscripts m and im denote the mobile and immobile domain respectively. The relative concentration difference between the domains drives the transfer of mass

$$\theta_{im} \frac{\partial c_{im}}{\partial t} = \alpha \left(c_m - c_{im} \right) \tag{2}$$

where α controls the rate of exchange between the domains $\left[T^{-1} \right]$. The mass transfer rate α has been derived using Fick's first law, and is used to represent diffusion over a length scale (e.g., Goltz and Roberts, 1986; Parker and Valocchi, 1986; Brusseau et al., 1991; Brusseau et al., 1994):

$$\alpha = \frac{D^*}{l^2} \tag{3}$$

where D^* is the aqueous diffusion coefficient $\left[L^2 T^{-1} \right]$. Here, l is representative of either the diameter of particles comprising the immobile domain or a length scale of mixing between the two domains (e.g., Haggerty and Gorelick, 1995; Griffioen et al., 1998).

The MIM formulation divides the flow field into advective and no-flow regions and has been applied successfully to solute transport problems using both conservative tracers and reactive tracers in a variety of hydrogeologic settings (e.g., van Genuchten and Wierenga, 1976; Cameron and Clute, 1977; Haggerty and Gorelick, 1994; Jardine et al., 1999; Gwo et al., 2007). One of the benefits of the MIM model is that the fitting parameters θ_m, θ_{im} and α may be related to and therefore constrained by porosity, particle size, diffusion coefficients, and/or geophysical measurements (e.g., Brusseau et al., 1994; Vanderborght et al., 1996; Casey et al., 1999; Al-Jabri et al., 2002; Lee et al., 2000; Singha et al., 2007; Luo et al., 2008, Gong et al., 2010). This approach lends itself to broad applicability; however, the assumed velocity partitioning into flowing and not-flowing zones is not an accurate representation of the true velocity field, and furthermore, a single mass transfer rate fails to match BTCs with particularly long tails (e.g., Haggerty and Gorelick, 1995; Gao et al., 2009). The MIM model is a highly restricted case of the continuous time random walk (CTRW) formalism, described below.

CTRW is an approach based on the conceptual picture of tracer particles undergoing a series of transitions, characterized by a distribution of transition times. The physics and/or geochemical mechanisms involved in the transport process, as well as the structure of the heterogeneous porous medium or nature of the flow regime, determine the relevant transition time distribution and control the interpretation of its parameters. In the CTRW framework, a solute particle undergoes a series of transitions of length **s** and time *t*. Together with a master

equation conserving solute mass, the random walk is developed into a transport equation in partial differential equation form. For a concise derivation starting from a simple random walk and leading to the transport equation, and an extensive review of CTRW, see Berkowitz et al. (2006). The transport equation in Laplace space, £, (denoted by ~ and Laplace variable u) is

$$u\tilde{c}(\mathbf{s},u)-c_0(\mathbf{s})=-\tilde{M}(u)\left[\mathbf{v}_\psi\cdot\nabla\tilde{c}(\mathbf{s},u)-\mathbf{D}_\psi:\nabla\nabla\tilde{c}(\mathbf{s},u)\right] \qquad (4)$$

where $\mathbf{v}_\psi=\dfrac{1}{t_1}\int p(\mathbf{s})\mathbf{s}\,d\mathbf{s}$ is an average tracer transport velocity, $\mathbf{D}_\psi=\dfrac{1}{t_1}\int\dfrac{1}{2}p(\mathbf{s})\mathbf{s}\mathbf{s}\,d\mathbf{s}$ is a generalized dispersion tensor, $p(\mathbf{s})$ is the probability density function (pdf) of the transition lengths, $\tilde{M}(u)=t_1u\dfrac{\tilde{\psi}(u)}{1-\tilde{\psi}(u)}$ is a 'memory' function and t_1 is characteristic transition time (Berkowitz et al. 2006 and references therein). Note that v_ψ is distinct from and therefore need not equal the fluid velocity, and for $0<\beta<1$, v_ψ scales as $t^{\beta-1}$ (see Berkowitz et al., 2006). Here we solve the 1-D form of Equation 4.

The pdf $\psi(t)=£^{-1}(u)$ is defined as the probability rate for a transition time t between sites. Its determination lies at the heart of the CTRW as it controls the nature of the transport. The truncated power law (TPL) form of $\psi(t)$ has been applied successfully to a wide range of physical scenarios (Berkowitz et al. 2006); the 'cut-off' of the power law allows a transition from anomalous behavior to Fickian behavior at longer times. The TPL form can be written as

$$\psi(t)=\frac{n}{t_1}\frac{e^{-t/t_2}}{\left(1+\dfrac{t}{t_1}\right)^{1+\beta}}\ ,\ 0<\beta<2 \ \text{where}\ n=\left[\left(\frac{t_1}{t_2}\right)^\beta e^{\frac{t_1}{t_2}}\Gamma\left(-\beta,\frac{t_1}{t_2}\right)\right]^{-1}$$ is a normalization factor, β is a

measure of the dispersion, t_2 $(\gg t_1)$ is a 'cut-off' time and $\Gamma(a,x)$ is the incomplete gamma function. Note that $\psi(t)\sim(t/t_1)^{-1-\beta}$ for $t_1\ll t\ll t_2$, and decreases exponentially $\psi(t)\sim e^{-t/t_2}$ for

$t >> t_2$. Fickian transport occurs for $\beta > 2$, while the smaller β is, the more dispersive the transport. A recent study sheds more light on the choice of these parameters and their interpretation in the context of flow velocity-dependent tailing (Berkowitz and Scher, 2009).

The CTRW concept of transport has few restrictions and can therefore quantify a wide range of non-Fickian transport patterns. CTRW has been applied successfully in many different settings (e.g., Berkowitz and Scher, 1998; Deng et al. 2008). Significantly, it consistently captures BTC behavior in column experiments of even well-sorted materials, where conventionally predicted classic advective-dispersive behavior does not always occur (Berkowitz et al. 2000; Cortis and Berkowitz, 2004). In most cases, the transport behavior can be quantified effectively with a single transition time distribution (Berkowitz and Scher, 2009); however, if there is clear evidence for the nature of the underlying transport mechanisms, an explicit two-scale CTRW formulation (Bijeljic et al., 2010) or a fully coupled space-time distribution may also be considered (Dentz et al., 2008).

Our understanding of the physical environment is shaped by the assumptions within our models. For example, interpretations from a MIM model assume the existence of a dual-porosity network that may or may not exist, whereas modeling the same dataset with a classic ADE model may only suggest that the subsurface is highly heterogeneous. In each case we can only infer actual behavior given concentration histories. We explore two conceptual models—CTRW and a simplified version of CTRW, the MIM model—with the goal of developing consistent interpretations of the subsurface hydrogeology.

FIELD SITE AND EXPERIMENTAL METHODS

Location and Site Details

The SH-CZO is an 8-hectare v-shaped catchment containing one first-order stream located in Huntingdon County, Pennsylvania within the Valley and Ridge physiographic province of the Appalachian Mountain Front (Figure 1). The SH-CZO is underlain almost entirely by the Silurian Rose Hill Shale. The Rose Hill Shale extends across much of the Appalachian Basin; locally, the Rose Hill Shale is a yellow-brown, olive to blue-gray fossiliferous shale marked by well-developed fracture cleavage (Flueckinger, 1969).

The resultant residual and colluvial silt-loam soils are well drained and contain many shale fragments (Lin et al., 2006). Five soil series have been identified within the catchment, the Berks, Weikert, Rushtown, Blairtown, and Earnest Series (Lin, 2006). Experiments were carried out on soils retrieved from the valley bottom within the Earnest soil series, a fine-loamy, mixed, superactive, mesic Aquic Fragiudults consistent with US Soil Taxonomy (Lin and Zhou, 2008). For additional details on soil distribution and descriptions, climate and hydrologic information, and geochemical composition across the catchment, see Lin (2006) and Jin et al. (2010). We follow the terminology introduced in Jin et al. (in press) to characterize the soil profile. The soil profile includes the regolith and saprock. Regolith is the near-surface disaggregated and highly altered material extending to a depth that can be reasonably sampled using a hand auger. Below the regolith lies the saprock, which is somewhat fractured and altered in-place bedrock. Chemically unaltered, in place, and less-fractured shale we denote as bedrock. The soil samples are collected in the regolith and saprock, while the field tracer experiment occurs in the transition zone between the saprock and bedrock. This soil profile, including regolith and saprock, extends approximately 1-3 m below land surface depending on location in the valley floor.

Near the outlet of the catchment within the valley floor a set of shallow boreholes (~16 m) was drilled and geophysical logs were collected in each (Figures 2,3). Drill cuttings and well log data reveal a calcareous-rich slow drilling zone around 6-7 m below land surface, above which is a poorly developed soil and highly weathered shale with comparatively high fracture density, and beneath which is a less-fractured, and rather geochemically homogeneous, blue-grey shale (Figure 3). Additionally, low natural gamma rays in the upper ~7 m of the boreholes indicate a removal of clay-rich materials and deletion of the parent bedrock material (Figure 3).
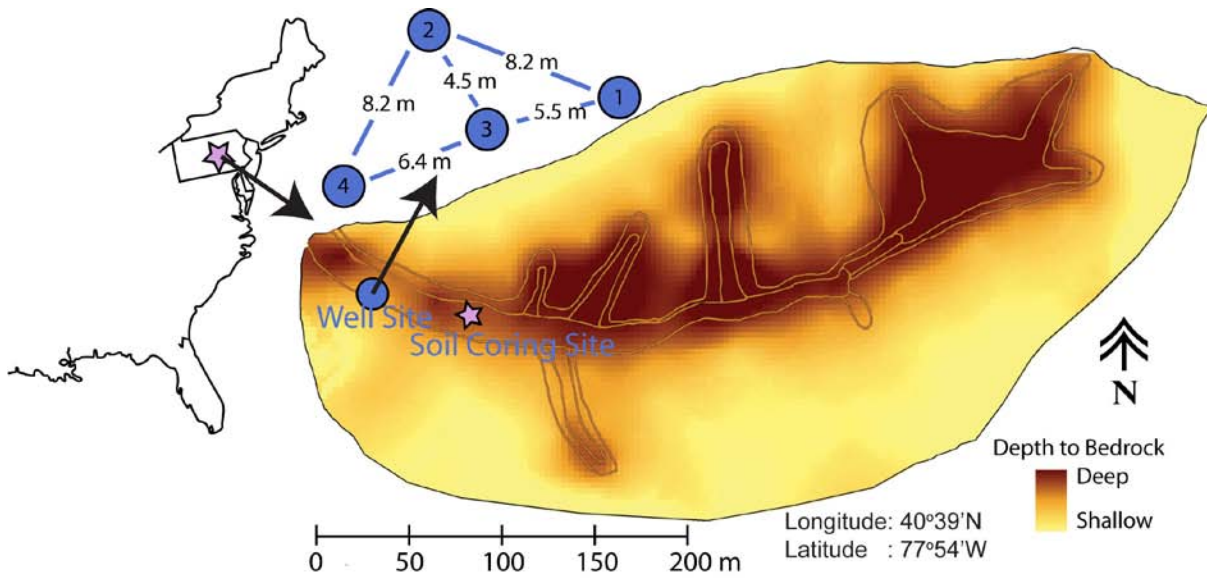
Figure 1. The well field and soil-core retrieval localities within the SH-CZO (after Lin et al., 2006). Soil depth is greater than 2 m in the valley floor and less than 0.3 m at the ridge tops. Critical Zone Monitoring Wells (CZMW) 1, 2, and 3 are located north of the stream and CZMW 4 is located south of the stream at the point-labeled well site. The field tracer test injected NaBr into CZMW 3 and extracted and sampled the tracer breakthrough at CZMW 2. Natural groundwater flow direction is approximately southeast to east.
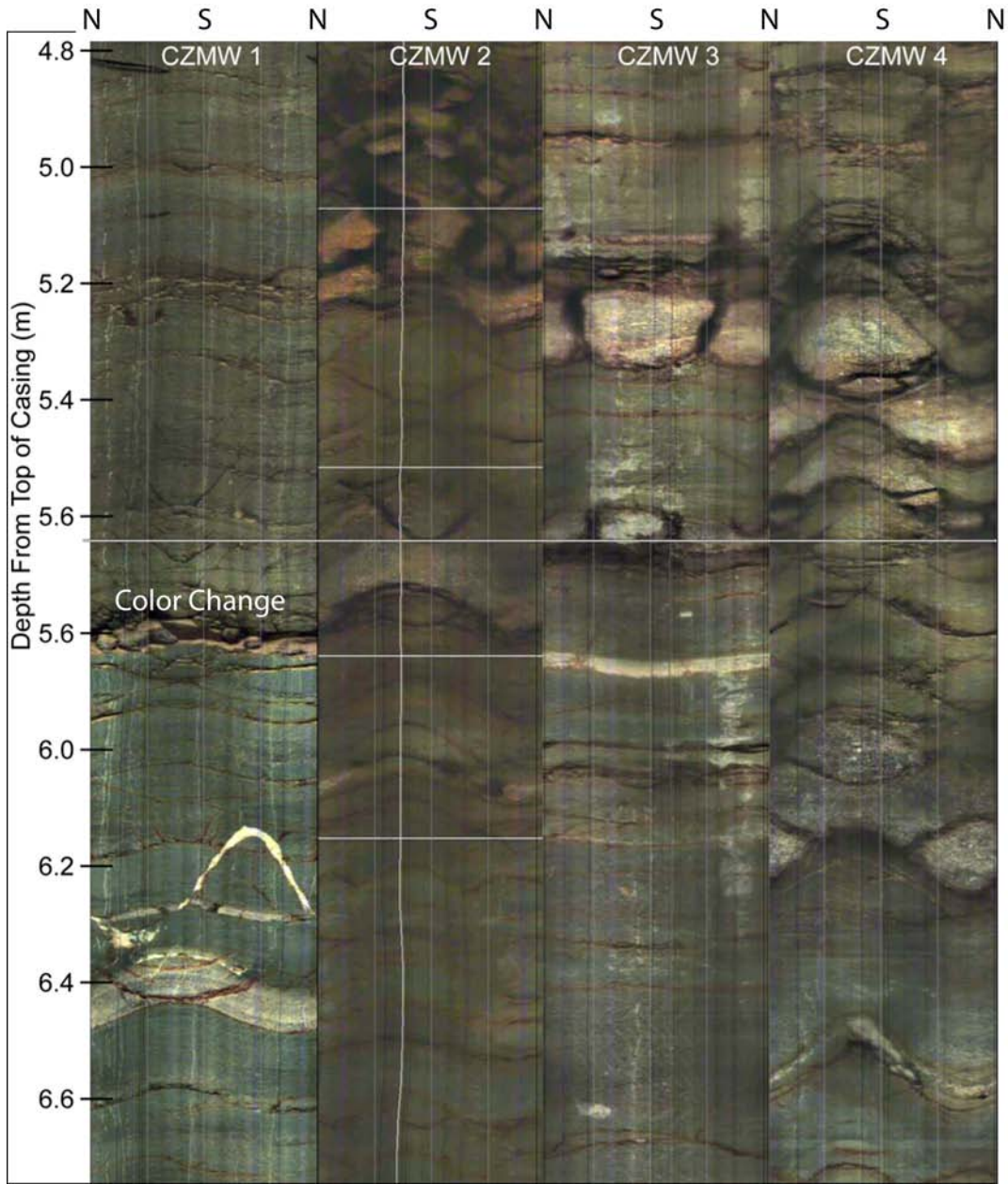
Figure 2. Optical televiewer log of the four 16-m deep Critical Zone Monitoring Wells (CZMW). Above approximately 6 m the shale bedrock is olive-brown to yellow-brown whereas below this depth the shale is fractured and blue-gray in color, as seen most clearly in CZMW1 above. Fracturing is greatest above 6 m, and decreases with depth (not seen here). These logs reveal that, on average, bedding strikes to the southeast ~230° and dips to the northwest 25 to 30°.
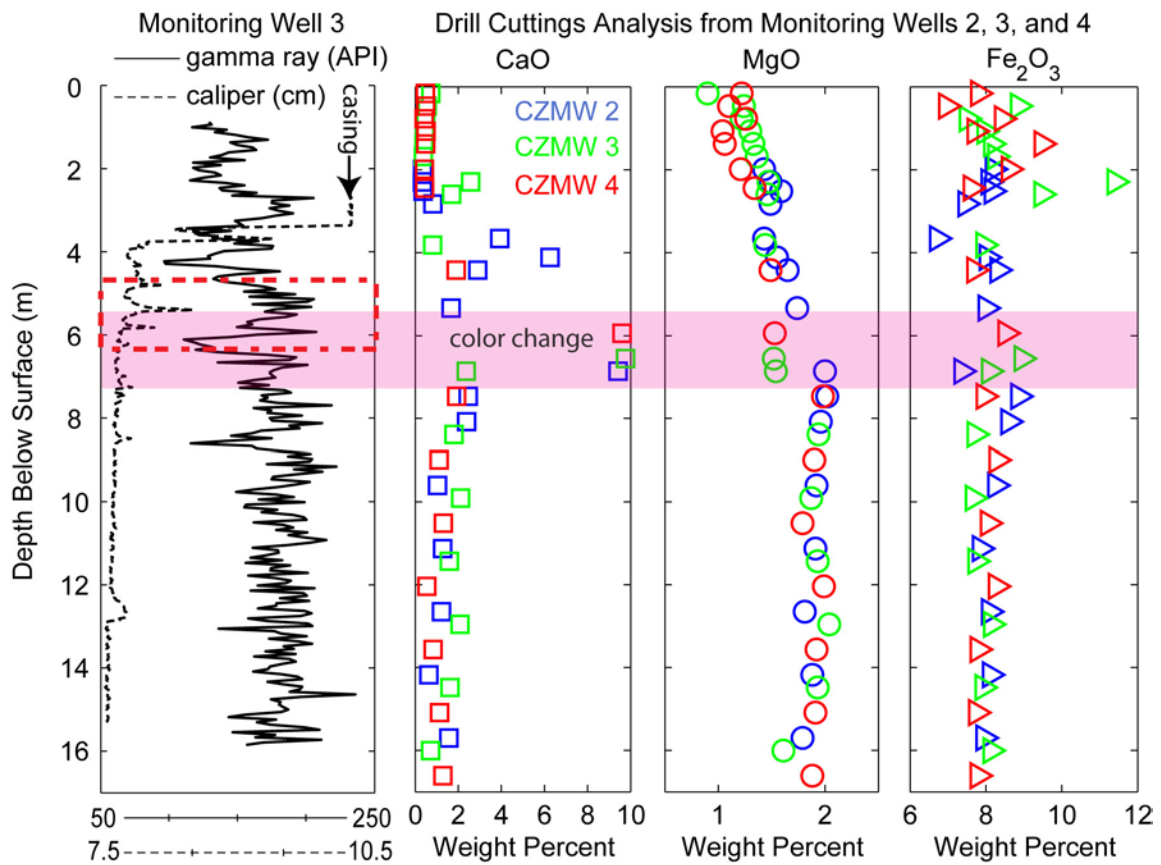
Figure 3. Natural gamma ray, three-arm caliper logs from CZMW 3, and chemical analysis from drill cuttings from CZMWs 2, 3, and 4. Gamma curves for all four wells were collected and have a distinctly similar character to CZMW 3. A calcareous-rich zone around 6 m correlates to a slow drilling zone and marks the transition between less-weathered and more-weathered shale as evidenced by 1) depletion of CaO and MgO, 2) an increase in fracture density, and 3) a decrease in the relative clay content as recorded by the natural gamma. The dashed rectangle on CZMW3 denotes the region where the tracer was injected into the subsurface.

Relatively undisturbed samples were collected from across the ~3 m deep soil profile with 7.6 cm diameter Shelby Tubes ~60 m east of the well site (Figure 1) within the toe slope of the valley floor. Shelby Tubes were hydraulically pressed into the soil using a tracked Geoprobe (Geoprobe® Model 6620DT). Because of the many rock fragments in the soil, in addition to hydraulically pressing, deeper Shelby Tubes were lightly hammered by the Geoprobe to reach the targeted soil depths. Field-sampled core lengths varied from 15 – 75 cm as permitted by soil conditions. Within eight hours of removal, samples were capped and stored in a 10 ^{o}C walk-in storage cooler. An additional set of 5.08-cm diameter samples were collected in clear acetate liners to visually inspect the soil color, texture, and particle size and composition with depth. This visual inspection helped us target four distinct zones for tracer experiments.

Physical and Hydraulic Properties

Hydraulic conductivity was measured in the Shelby tube samples by both constant-head and falling-head methods. One end of the samples was prepared with porous sintered-metal frits (bubbling pressure <20 cm) to distribute pressure evenly across the base of the sample. Total porosity was measured on 4-7 cm subsections of the Shelby Tubes adjacent to the sections used for transport experiments. Samples were fully saturated with 5 mM calcium chloride ($CaCl_2$) under vacuum, weighed, and subsequently dried at 40 ^{o}C until no significant change in mass occurred between measurements. To investigate the porosity and permeability of the shale bedrock matrix we sampled the Rose Hill Shale from a nearby outcrop (~15 km NE, latitude: 40° 42' 9.71" N, longitude: 77° 43' 24.22" W). Porosity was estimated by mercury porosimetry (measured by Porous Materials Inc.; Ithaca, NY). Permeability was measured on the consolidated Rose Hill Shale via curve matching with the transient pulse-decay method (Brace et al., 1968; Hsieh et al., 1981) in a triaxial pressure apparatus. Pressure at one end of the sample

was instantaneously pulsed with 300 kPa and then allowed to equilibrate across the sample. Pressure was monitored for the decay and the increase from the pulse at the upstream and downstream sides of the sample, respectively. Theoretical curves were then matched to the data until the error is minimized.

Particle size distribution data were analyzed on regolith and saprock from the Shelby tube samples at various intervals across the soil profile. Analysis was performed by wet sieving rock large (>6.35 mm) and (6.35-2.00 mm) small fragments, sand sized particles, and assuming silt- and clay-sized particles comprise the remainder of the sampled material. Drill cuttings from each of the boreholes were ground and analyzed for major cation concentration in the geologic media by inductively coupled plasma atomic emission spectroscopy (Penn State Materials Characterization Laboratory).

Column Tracer Experiments

Strontium bromide ($SrBr_2$) tracer experiments were carried out on four Shelby Tube cores sampled from depths of 0-0.20 m, 0.60-0.80 m, 1.6-1.8 m, and 2.3-2.5 m. Shelby Tube samples were carefully cut with the aid of a low-speed bandsaw into 19.5 ± 0.5 cm sections from the larger field-recovered cores. Chlorinated polyvinyl chloride (CPVC) caps were prepared for each core by filling the convex top with an impermeable epoxy to eliminate dead volume between sample and cap. One brass tube fitting was fixed into the center of each cap, and caps were secured to the sectioned Shelby Tube core with adhesive; a porous sintered disk was placed at the inlet boundary between sample and cap to distribute solute and pressure evenly across the sample. Soil cores were then inverted and flow was directed from the base to the top of the sample to represent vertical 1D flow down through the soil. Fluid delivery was provided by Cole Parmer Masterflex L/S drive with a six-channel pump head (7519-15). To minimize diffusion

within the line before entering the geologic media, a three-way valve was placed at the base of the sample to switch between background influent and tracer solution. Effluent fluid conductivity (EC) was monitored continuously by an inline conductivity meter (Campbell Scientific Model 542). Flow rate was measured regularly. 5 mM $CaCl_2$ (fluid conductivity = 1.2 $\pm$ 0.2 mS/cm) background solution was pumped through the cores for several days (30+ pore volumes) until flow rate and EC stabilized; we chose this solution to minimize the impact of the small fraction of swelling clays (vermiculite) within the sample. $SrBr_2$ was added to the prepared background $CaCl_2$ solution creating a 5 mM $SrBr_2$ tracer solution (fluid conductivity = 2.3 $\pm$ 0.2 mS/cm). Each core was saturated with 3-5 pore volumes of $SrBr_2$ tracer before reintroducing background $CaCl_2$ solution. Intermittently, effluent was allowed to drip into 20 ml scintillation vials for bromide analysis. Water samples were diluted and bromide concentrations were measured on an ICS 2500 Dionex ion chromatography system, using an IonPac AS18 column with an isocratic 39 mM KOH elution program at a flow rate of 1 ml/min and an oven temperature of $31°C$. In this paper, we analyze only the bromide data to examine the physical transport processes.

Field Tracer Test

A modified doublet tracer test was performed between Critical Zone Monitoring Well (CZMW) 3 and CZMW 2, which are 4.5 m apart (Figure 1). Tracer was injected at CZMW 3 into a packed-off zone between 5 and 6 m below land surface. Extraction occurred in CZMW 2, which is an open wellbore 10 m long with the pump placed at 0.5 m from the bottom. The test was set up as a doublet for the first 700 minutes; after this period only the extraction well was utilized. Injection of fresh water (EC = 300 $\pm$ 20 µS/cm) occurred for 40 min to establish steady-state, followed by 150 min of saltwater injection (10 g/L NaBr, EC = 14.2 mS/cm), which was

followed again by fresh water injection for 550 min. The injection rate was constant at 1.7 L/min. The extraction well ran continuously at 2 L/min for the entirety of the test, plus an additional 1440 min after the injection well was turned off. The natural flow gradient of 0.04 is nearly parallel with bedding strike, which is approximately perpendicular to the direction the injection-extraction well orientation (Figure 1).

MIM Solute Transport Modeling

We created a 1-D finite-element transport model with the MIM framework using the Earth Sciences Solute Transport (ESST) module of COMSOL Multiphysics software. Initial and boundary conditions of the forward simulations were dictated by experimental conditions. Solute concentration within the mobile domain is controlled by Equation 1 and mass is exchanged between that domain and the immobile domain by Equation 3. To create an immobile pore space using COMSOL, we implemented two solute transport modules, one with a fluid velocity (Equation 1) and one in which the velocity and the dispersion coefficient is set to zero (Equation 3).

Specific discharge defined by $q = \dfrac{Q}{A}$, where Q is effluent discharge $\left[L^3 T^{-1} \right]$ and A is the area of column $\left[L^2 \right]$, dictates the flux input to the model domain. A Dirichlet boundary condition is used at the inlet boundary, which sets the concentration to a step-function of time $c = c(t)$, reflecting the switch between background solution ($CaCl_2$) and tracer solution ($SrBr_2$) in the mobile domain; and $c = 0$ for all t within the immobile domain. The outlet boundary is an advective-flux condition or free boundary which neglects transport by diffusion perpendicular to the boundary, defined by $n \left(\theta D \dfrac{\partial c}{\partial x} \right) = 0$, where n is the vector normal to the boundary.

Field tracer breakthrough was also modeled using a 1D approach similar to the columns. Flux input was estimated by calculating the advective velocity from the mean arrival time of the tracer breakthrough at the extraction well and assuming a porosity of 0.035, which was obtained from porosimetry measurements.

Goodness of MIM fit to each BTC was determined by first matching the mean arrival time $c/c_0 = 0.5$ with dispersivity and mobile porosity using the ADE. After this, we fixed dispersivity, and constrained the total porosity of the model by the measured porosity $\theta_T \simeq \theta_m + \theta_{im}$ to determine the immobile porosity, and finally plotted the solutions in log-log space to examine the tailing. In addition to this fitting "by eye" approach, we also ran several additional forward models and calculated the root mean squared error (RMSE) to analyze the sensitivity of θ_m, θ_{im}, and α parameters and determine the range of values that will adequately represent transport behavior (see Appendix B). The RMSE is a useful tool to estimate overall fit and has been used to estimate solute transport parameters from BTCs (e.g., Toride et al. 1999); however, because the RMSE disproportionally weights very large differences between model and measured data the lowest RMSE values may not provide the best fit to the observed tailing behavior, where differences between model and measured data are small. We therefore determine the goodness of the MIM fit and based on the combination of calculating the RMSE, examining the percent error between model and data over the entire simulation, and utilizing log-log space to determine the goodness of the fit to the late time data.

CTRW Solute Transport Modeling

For the 1-D, CTRW Model, the initial condition is $c_r(x, t = 0) = 0$ where c_r is the resident concentration. The inlet boundary condition is a Robin type, i.e.,

$\tilde{c}_r \left(x = 0, u \right) - \dfrac{D_\psi}{v_\psi} \left[\dfrac{\partial \tilde{c}_r}{\partial x} \right]_{x=0} = 1$, where '~' denotes the Laplace space quantity and u is the

Laplace variable, and the outlet boundary condition is a Neumann type, i.e., $\left[\dfrac{\partial \tilde{c}_r}{\partial x} \right]_{x=0} = 1$.

RESULTS

Porosity and Hydraulic Conductivity

Soil porosity and hydraulic conductivity both decrease from regolith to saprock. The uppermost regolith has a total porosity of 0.44, and saprock has a porosity θ_T of only 0.34 to 0.29 (Table 1). Hydraulic conductivity also has a deceasing trend with increased soil depth, reducing by three orders of magnitude over the soil profile from 5.8×10^{-6} m/s at the top to 2.3×10^{-9} m/s at a depth of 2.5 m (Table 1). Lin (2006) also measured hydraulic conductivity on the Earnest soils down to a depth of 1.37 m, observing fairly constant hydraulic conductivity measurements of $\sim 10^{-5}$ m/s. However, values reported for weathered shale saprolite commonly have hydraulic conductivities in the $10^{-6} - 10^{-9}$ m/s range (e.g., Mayes et al., 2000).

Hydraulic conductivity and porosimetry measurements on the consolidated Rose Hill Shale matrix, collected offsite as noted previously, yield a very low hydraulic conductivity of 2.7×10^{-15} m/s and a porosity of 0.035 (Table 1). Neuzil (1994) identified a log-linear relationship between porosity and permeability for shales and clay-rich materials from numerous laboratory datasets, and the measured porosity and permeability of the Rose Hill Shale falls within the lower limits of this permeability-porosity relationship. Porosimetry data show that only about 15% of the shale matrix is composed of pore throats greater than 0.1 μm with the largest 1% of the pore throats reaching 2 or 3 μm (Figure 4). In contrast to the shale matrix, several slug tests and pumping tests performed in the boreholes suggest that the lowermost saprock and bedrock at the SH-CZO have a relatively high hydraulic conductivity, upwards of 10^{-6} m/s.

Table 1. Physical properties of laboratory- and field-scale experiments and experimental setup.

depth [m]	θ_T	K_{sat} [m/s]	Injection Period [d]	Flux, q [cm/d]
0-0.2	0.44	$4.9 – 58 \times 10^{-7}$	0.54	66
0.6-0.8	0.34	$1.8 - 2.7 \times 10^{-7}$	0.45	63
1.6-1.8	0.29	$1.3 – 1.7 \times 10^{-8}$	0.81	29
2.3-2.5	0.29	$1.3 – 2.3 \times 10^{-9}$	0.58	37
5-6	-	$\sim 10^{-6}$	0.08	-
Shale	0.035	2.7×10^{-15}	-	-
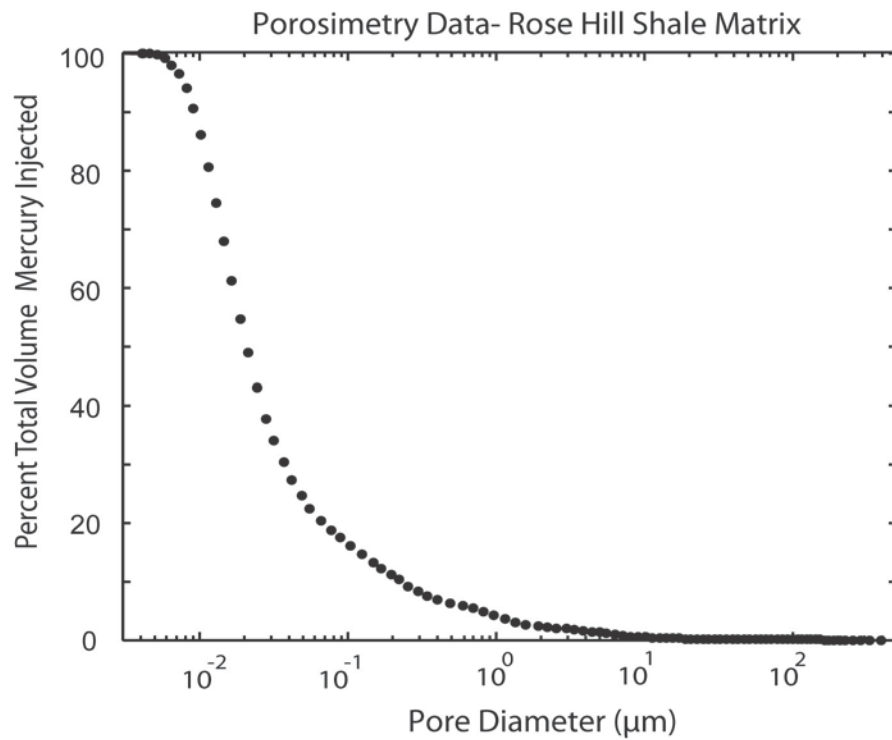
Figure 4. Mercury porosimetry results performed on a consolidated, unfractured Rose Hill Shale sample. Total calculated porosity for the sample, based on these porosimetry data, is 0.035.

Profiles observed in caliper and optical televiewer logs (Figures 2, 3) suggest that the primary or short-term controls on groundwater flow are secondary structures such as bedding planes, fractures, and preferential pathways, rather than the low-permeability matrix. Simulating groundwater flow and transport in fractured rock provides a substantial challenge given the wide ranges of hydraulic conductivity over a short interval. Fracture sets in rock typically occur as groups of tens to thousands of individual fractures, though only a small proportion of those may be relevant for conducting fluids (e.g., Long et al., 1991; Renshaw, 1995; Hsieh and Shapiro, 1996). The lack of spatial and hydrologic resolution of the fracture network at the SH-CZO limits our ability to simulate flow using a discrete fracture network.

Complicating efforts to predict solute transport in fractured media is a fundamental uncertainty regarding the physical processes at work. For example, long tails on solute breakthrough curves can be attributed to either rate-limited mass transfer between fractures and matrix (Grisak et al., 1980; Neretnieks, 1980; Rasmuson and Neretnieks, 1986) and/or the existence of multiple advective pathways of differing velocity (Becker and Shapiro, 2000; 2003). Here we observe that the majority of the pore diameters within the shale are less than a 0.1 μm, providing the capacity to store solutes, but being less likely to permit advection. Assuming diffusion controls the transfer of mass between these small pores and the adjacent advective pathways, we expect such processes could contribute to transport processes on long time scales. Macropores and preferential flow paths are also inferred from high spatially resolved soil-moisture data in the catchment (Lin, 2006). Given the large range in hydraulic conductivity, presence of macropores, and variability in porosity at the SH-CZO, we might expect BTCs from both the soil and aquifer to be asymmetric, having earlier-than-expected breakthrough times and

exhibiting tailing behavior due to rate-limited mass transfer and variable or multiple advective pathways.

Model Analysis

Figure 5 depicts electrical fluid conductivity (EC) together with bromide concentrations (Br) in addition to ADE, MIM, and CTRW model solutions for the soil core tracer experiments. Each BTC is characterized by early breakthrough and tailing. The results are presented on a log-log plot which allows detailed examination of the BTC tailing. Values for ADE, MIM, and CTRW fitting parameters are listed in Tables 2, 3. The MIM soil core parameters in conjunction with soil properties are plotted as a function of soil depth in Figure 6. While the ADE can, in most cases, match the mean breakthrough time it fails to match the observed tailing behavior. Additionally, the ADE consistently reaches $c/c_0 = 1$ during breakthrough, while observed maximum breakthrough is $c/c_0 = 0.95 \pm 0.02$. Therefore the ADE is predicting steady state before we observe such a state in the measured data. Because the ADE fails to match much of the observed tracer transport behavior we focus our analysis on the CTRW and MIM modeling results.
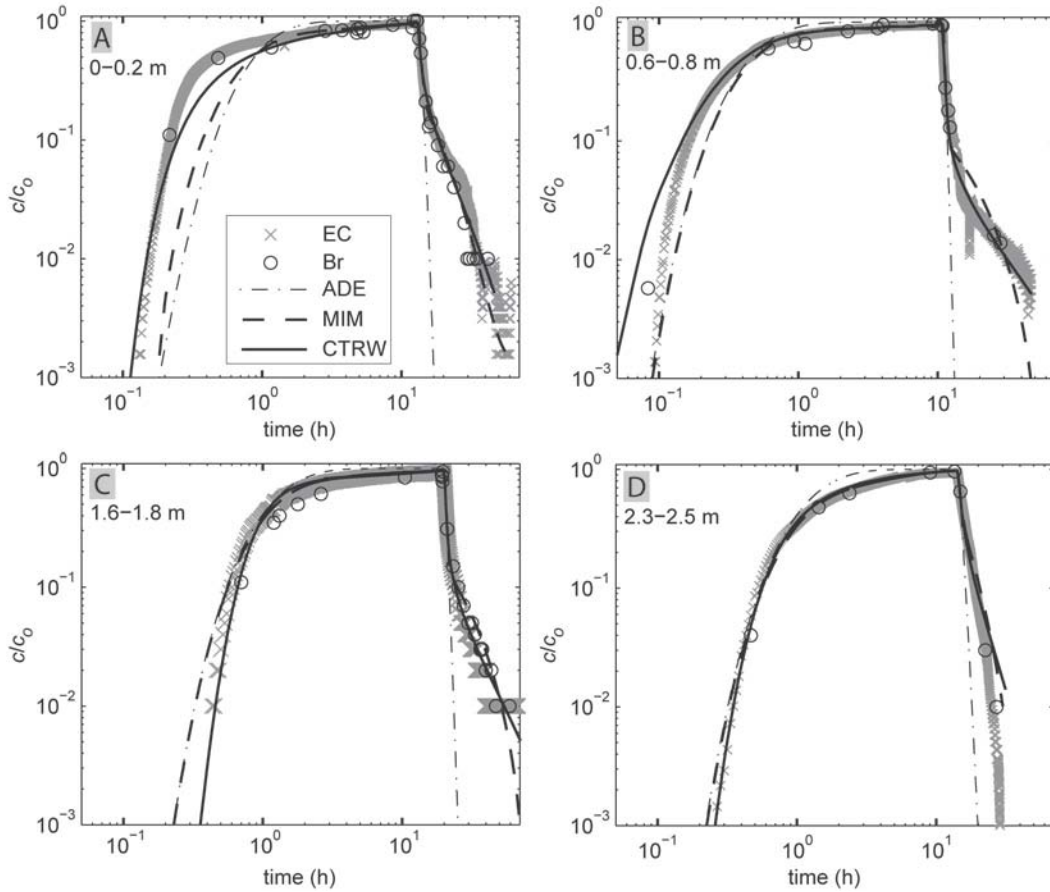
Figure 5. Measured BTCs with ADE, MIM, and CTRW solutions for soil cores from soil coring site at depths of (A) 0-0.2 m, (B) 0.6-0.8 m, (C) 1.6-1.8 m, and (D) 2.3-2.5 m depths. EC = effluent conductivity, Br = measured bromide concentration plotted as c/c_0 where c_0 is the influent concentration.
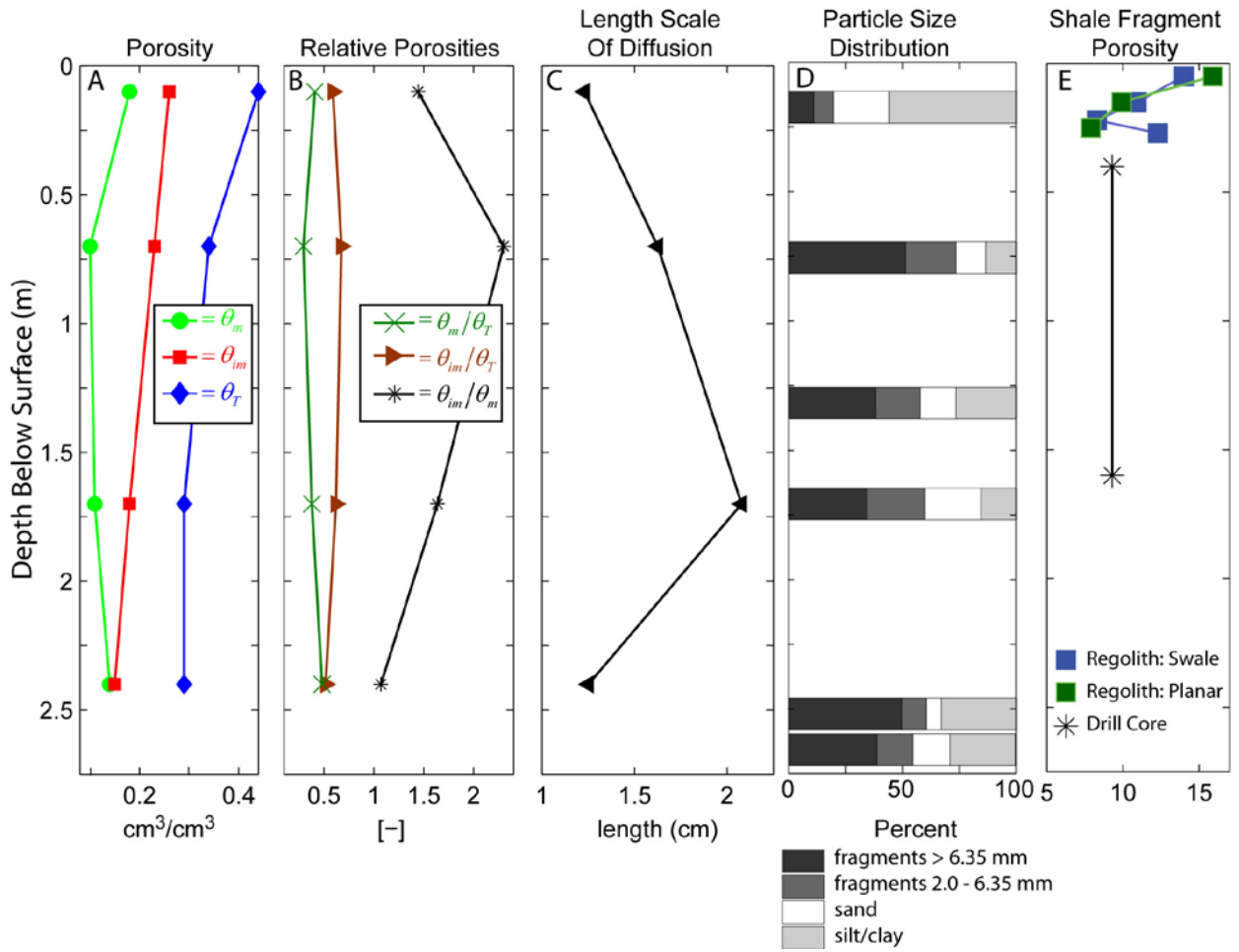
Figure 6. MIM modeling results and physical soil properties plotted against soil depth, including (A) fit values for mobile and immobile porosity, (B) relative porosities (C) estimated length scale of diffusion using Equation 3, (D) PSD data from various sections in the soil profile, and (E) porosity measurements on Rose Hill Shale fragments from various depths at different locations along ridge top of the SH-CZO (modified from Jin et al., in press).

Table 2. Best-fit ADE and MIM parameters used for fitting
laboratory- and field-scale data

depth [m]	$^{\dagger}\theta_m$	θ_{im}	θ_m/θ_T	α [d^{-1}]	$^{\dagger}\gamma$ [m]
0-0.2	0.18	0.26	0.41	1.17	0.035
0.6-0.8	0.10	0.23	0.30	0.67	0.05
1.6-1.8	0.11	0.18	0.38	0.41	0.05
2.3-2.5	0.14	0.15	0.48	1.13	0.052
field	0.045	0.08	0.36	0.30	0.50

†ADE and MIM Parameter, γ = dispersivity

Table 3. Best-fit CTRW parameters used for fitting laboratory- and field-scale data.

depth [m]	v_{ψ} [cm/s]	D_{ψ} [cm^2/s]	β	t_1 [s]	t_2 (d)
0-0.2	9.84×10^{-2}	6.86×10^{-3}	0.91	3.31	1.11
0.6-0.8	1.35×10^{-1}	7.58×10^{-1}	1.05	1.0×10^{-3}	9.19
1.6-1.8	6.0×10^{-2}	4.0×10^{-2}	1.01	1.26×10^{-2}	3.66
2.3-2.5	5.4×10^{-2}	1.6×10^{-2}	0.91	2.19	0.73
field tracer	3.35	2.87	0.83	6.19×10^{-1}	2.69×10^{3}

Figure 5A shows the results of the shallow regolith core from a depth of 0 to 0.2 m. The

breakthrough is fast and CTRW captures this behavior better than the ADE or MIM models. The

tail is fit well by CTRW with the parameter β=0.91, which is consistent with strong anomalous

transport. The characteristic transition time t_1 in this case is high, which allows a good fit to the

fast breakthrough observed. The average tracer velocity is ~50 times faster than the measured

fluid velocity. This finding is consistent with the fast breakthrough of solutes (arriving before 1

pore volume) and may indicate fast channeling for solute migration in the strongly

heterogeneous domain, and is corroborated by the relatively low β value. From the MIM

analysis, approximately 60% of the total pore space is immobile, and mass transfer between the

mobile and immobile domain is fast relative to the rest of the soil cores. This shallow core

deviates from the rest of the soil cores by having significant amounts of silt and clay sized

particles containing far less rock fragments than deeper soil cores (Figure 6D). The late-time

tailing behavior is represented well by both MIM and CTRW.

     Data from a core of depth 0.6-0.8 m are presented in Figure 5B. CTRW captures the early

breakthrough of bromide, which deviates from the EC measurements in this case. CTRW best

describes the tailing shape observed in the EC record with a β of 1.05. CTRW parameters for

this soil core are considerably different from all other cores, with high solute velocity v_ψ,

dispersion D_ψ values, and a short transition time t_1 (Table 3); these point to a transport regime

affected by preferential flow paths or fractured rock. These results are consistent with the

particle size distribution (PSD) data, which indicate that ~75% of the 0.6-0.8 m core is composed

of rock fragments (Figure 6D). Similarly, MIM results deviate from the rest of the soil cores

with a low mobile porosity and low mass transfer rate indicating restricted advective pathways

and the potential to store solutes longer than the adjacent soils. The MIM solution does not

match the change in slope at ~15 h and tailing during late time well, in contrast to the CTRW solution.

Figure 5C shows the results from the core at depth 1.6-1.8 m. In this case only CTRW captures the anomalous early breakthrough as well as the long tailing, with a best fit β of 1.01. The tracer velocity v_ψ is again ~50 times greater than the flow velocity and the dispersion D_ψ falls roughly between the other dispersion values. Low mass transfer coupled with low mobile porosity is also apparent in this soil core (Figure 6B, C). The significant late-time tailing behavior from this soil core is best represented by CTRW.

The BTC for the lowermost soil core does not exhibit the notable tailing observed in the intermediate soil cores but behaves more similarly to the upper most soil core (Figure 5D). CTRW matches the breakthrough portion of the curve exceptionally well with a v_ψ, D_ψ, and β similar to the 1.6-1.8 m soil core, while the transition time and cutoff times are quite similar to those of the uppermost soil core. The majority of the late-time tailing behavior is adequately captured by both CTRW and MIM.

The CTRW fit to the field data is notably better than the ADE and MIM results (Figure 7). The CTRW fitting parameters indicate a strongly anomalous transport behavior. Compared to the CTRW parameters of the core data analysis, β is slightly lower and t_2 is significantly larger than the typical values obtained for the laboratory-scale core data, indicating the dominance of the non-Fickian nature of the transport in the field scale. The inability of the MIM to match the breakthrough portion and long tail of the field data also attests to highly non-Fickian transport.
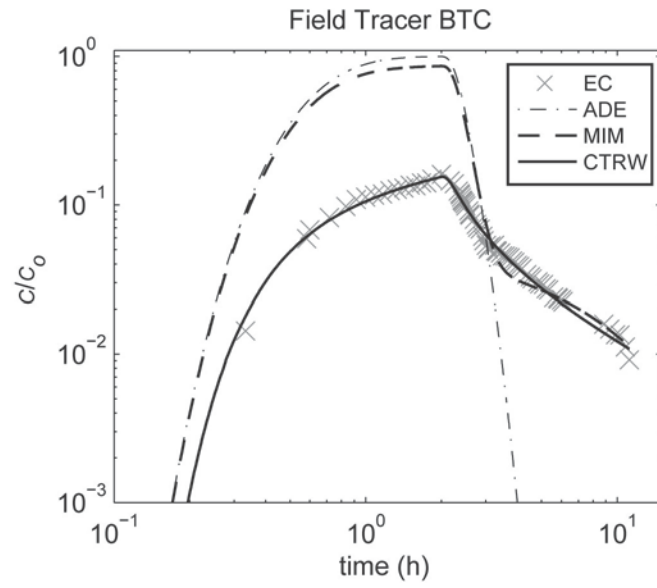
Figure 7. Field tracer BTC as measured at pumped well CZMW 2.

IMPLICATIONS AND DISCUSSION

MIM modeling of the soil core tracer experiments indicates trends that mimic those observed in the measured porosity and hydraulic conductivity in that MIM parameters tend to decrease with increased depth. Our results suggest that 1) solutes appear to be advecting in 30-50% of the total porosity vertically across the soil profile and 2) the fraction of immobile pore space decreases linearly with depth (Figure 6A). The low mobile porosity relative to the total pore space (<50%) signals the existence and control of preferential flow paths, consistent with similar MIM analysis of undisturbed soil cores (Seyfried and Rao, 1987). The effect of preferential flow may be especially important in the intermediate deeper regolith and saprock cores (0.6-0.8 and 1.6-1.8 m) where $\theta_m / \theta_T < 0.4$. In the regions of the soil profile dominated by aggregates we expect mass transfer to the less-mobile pore space to be controlled by diffusion (Griffioen et al., 1998).

MIM parameters for the soil cores may be indicative of physical properties related to weathering. The pattern of increasing immobile porosity from deep to shallow soil core (Figure 6A) may be due to increased weathering. This observation is supported by neutron porosity work by Jin et al. (in revision), which investigated the porosity of the shale fragments extending through the regolith and down into the bedrock. The porosity of the shale fragments is greater than 15% in the uppermost soils, decreasing to ~5% at depth. Jin et al. (in press) suggest that three pore types exist within the shale bedrock: 1) interlayer pores (pores between 2:1 clay layers), 2) intra-particle pores (pores between mineral assemblages), and 3) inter-particle pores (pores between particle boundaries), the smallest pores being the interlayer pores. The increase in porosity from weathering is thought to occur from the development of intra-particle pore space from the dissolution of clay. Lower natural gamma ray values at the surface measured in 16-m

deep boreholes near the catchment outlet attest to a reduction in clay content near the surface (Figure 3). Our modeling also indicates that immobile pore space decreases with depth of the soil profile, which may be associated with weathering of clay on the shale fragments in the shallow soils or reflect the changes in soil texture, particle size, and soil structure.

To examine the inferred relationship between porosity development from weathering and immobile porosity on the shale fragments, we examine the distribution of rock fragments within each of the measured soil cores (Figure 6D). PSDs collected by wet sieving reveal that rock fragments comprise 20-50% of the total soil composition, and greater than ~60% of those rock fragments are larger than 6.35 mm. Given that the porosity of the shale fragments is up to 3 times greater in shallow soils from the weathering of clay (Figure 6E), we suggest that the increased porosity of the shale fragments may be associated with the increased immobile porosity identified by the MIM modeling. Interestingly, the best fit mass transfer rates result in a length scale of diffusion on the order of centimeters, potentially reflecting the influence of large particles such as rock fragments (Figure 6C). The regolith and shallow saprock (soil cores 0-0.2 and 0.6-0.8 m) are well documented with large rock fragments (Figure 6D). Visual inspection also reveals that rock fragments in the upper three soil cores are olive-gray to yellow and sub-angular to rounded, whereas fragments from a depth 2.5 meters and greater are bluish-gray and angular to sub-angular, with only slight indication of weathering or alteration. The rock fragment composition change is consistent with observations by the optical televiewer and geophysical logs where shale bedrock changes from less weathered to more weathered below 6 m depth (Figure 2, Figure 3). Soil cores from 0.6-0.8 m and 1.6-1.8 m contain >60% weathered rock fragments and have relatively large immobile domains based on MIM modeling, suggesting a relationship between weathering of the shale fragments and immobile domain porosity. Tracer

tests from the deeper samples from the saprock show a mass recovery of ~95-98%, whereas the sample from within the regolith appears to have recovered nearly all of the injected mass. The trapped mass within the saprock samples attests to the retention of solutes within the shale fragment dominated media. Finally, rock fragments do not make up a large percentage of the shallow core, thus indicating that the structure of the immobile domain may be a combination of not only rock fragment porosity but also soil texture and composition.

With exception of the deepest soil core, the rate of mass transfer α also decreases with depth into the soil profile and aquifer, being ~ 1/d in the uppermost core and less than 1/d for soil cores from 0.6-0.8 m and 1.6-1.8 m (Table 2). These values of mass transfer are similar to Reedy et al. (1996) who also performed tracer experiments on an undisturbed shale saprolite core. A reduction in mass transfer rate with depth might be expected if the mass transfer rate is reflecting the increased length of mixing (Equation 3) or the increased heterogeneity encountered by the mobile and immobile domains (Haggerty and Gorelick, 1995). Koch and Fluhler (1993) point out simultaneously optimizing θ_m, θ_{im} and α could result in highly correlated parameters that have little physical meaning. For example, it is not clear how to interpret the characteristic length scale of diffusion, as defined in equation 3. The diffusion length scales estimated for the soil cores are on the order of centimeters, while >60 % soil is composed of small rock fragments (2-6.35 mm), sand, and silt sized particles. The diffusion length scale may reflect the fracture spacing, the presence of large rock fragments, or a combination of these physical properties. We note that it is difficult to determine the physical meaning of many of these fitted parameters, but that there is certainly correlation between physical properties and our estimated parameters. Failing to directly tie parameters such as mass transfer rates and diffusion scales directly to physical properties limits our ability to interpret solute transport behavior. However, we 1)

highlight a potential relationship between immobile pore space and rock fragments and 2) validate the prevalence of preferential flow paths throughout the entire soil profile using this modeling analysis.

The CTRW and MIM modeling confirm the heterogeneous nature of the regolith and shale-bedrock aquifer, offer insight on the architecture of the flow field, and help distinguish the operation of physical transport processes important to the SH-CZO. In both soil cores and the field scale we find anomalous early breakthrough and long tailing. The early breakthrough is consistent with the exceptionally high average solute velocity compared to the average fluid velocity, which results from the presence of strong preferential pathways. The highly anomalous nature of the transport observed by the long tailing is further confirmed by the low β values. However, unlike the MIM results we do not find a distinct trend of the CTRW parameters with soil core depth. In all cases presented here, the parameter t_2 indicates that the tracer injection experiment lies in the non-Fickian times; the power-law region of the TPL pdf, as t_2 is larger than the experiment duration. When the cutoff time t_2 is large the mass transfer rate required to capture the tailing behavior is low; and the goodness of the MIM model fit to the BTC diminishes (Figures 5B, C, 7). In these cases where the MIM results are less adequate (soil cores 0.6-0.8, 1.6-1.8 m and the field tracer) we observe immobile domains are greater than 1.5 times the size of the mobile domain and mass transfer rates are less than 1/d. This combination of low mass transfer rates, large immobile domains, and long cutoff times indicates the mass storage potential of the soil or aquifer matrix and suggests the need to incorporate more complex mass transfer processes such as a continuum of mass transfer rates. Gao et al. (2009) also recognized the inadequacy of MIM modeling and the ability of CTRW to match long tails in a large column of highly heterogeneous materials. Moreover, the MIM has the capacity to fit either the early

breakthrough or the tailing measured in the field, but cannot fit both sections of the BTC with one set of parameters. CTRW allows solutes to move separately from the fluid velocity and permits a slow release from storage via a distribution of mass transfer rates, providing a more complete representation of the solute transport behavior at the SH-CZO. However, performing CTRW analysis without incorporating a MIM analysis, one cannot estimate the size of that storage zone (immobile domain) or identify the timescale of mass transfer into and out of these storage zones.

Combining the CTRW and MIM analyses of the field tracer experiment we can conclude that solute transport in the aquifer is 1) not well represented by classic advection and dispersion, 2) a dual-domain system with a single mass transfer rate fails to capture both early breakthrough and long tailing behavior, and 3) the CTRW approach recreates the entire BTC with a parameter set, implying prevalent non-Fickian transport. Solute transport in certain sections of the soil profile and within the aquifer indicate more complicated behavior than simple linear mass transfer between two domains, including early breakthrough and significant long tailing. In such cases, CTRW more accurately matches the BTCs than MIM. Failing to incorporate the variability of parameters into groundwater age or soil weathering models would lead to an underestimated residence time of solutes in the catchment, because the rate limiting step of mass transfer in and out of stagnant water regions retains solutes within the system longer than models which contain only advection and dispersion.

CONCLUSIONS

Quantification of the operative solute transport processes across the entire soil profile and aquifer at the SH-CZO identifies controls on the residence time of solutes, clarifies the important role of preferential pathways in conducting fluid, and outlines how the composition of the regolith and aquifer contributes to the movement of solutes between more- and less- mobile domains. Additionally, we hypothesize that the MIM modeling results for the soil cores are indicative of soil properties and may reflect the effects of weathering on the soil profile. While the ADE can capture the mean arrival time of the BTCs, it consistently overestimates at peak concentration. Consistent discrepancies between the ADE and all measured BTCs imply that transport at the SH-CZO cannot be solely characterized by advection and Fickian dispersion processes. Best fit ADE models were found to require 1) a low effective porosity and 2) a large dispersivity value relative to the scale of the experiment.

Solute transport throughout the system cannot be ascribed solely to a simple mobile-immobile conceptualization. Solute transport in the soil and aquifer at the SH-CZO is characterized by highly non-Fickian behavior which in some cases is better described by a CTRW model than by a simple MIM. In the presence of low mass transfer rates, large immobile domains and long cutoff times, a continuum of mass transfer rates as described by CTRW was needed to match measured BTCs. With relation to geology, when the geologic media are largely composed of shale fragments and fractured rock the times required until Fickian behavior occurs tend to increase; and applying a single mass transfer rate may be an over simplification of the physical transport phenomenon. Moreover, allowing an average tracer velocity that is distinct from the fluid velocity permits a match to the very early breakthrough and late-time tailing.

Incorporating rate-limited mass transfer into groundwater age and soil weathering models at the SH-CZO is one way to account for the increased residence time of solutes in the fractured bedrock and silty-loam soils. Conceptualizing solutes undergoing a series of transitions in space and time independent of the flow regime may prove useful to evaluate the function of regolith at the SH-CZO. Here, combining CTRW and MIM results has helped to investigate the operative transport processes across a soil profile and within the fractured shale bedrock as a composite system. For example, the high tracer transport velocity v_ψ coupled with the low effective or mobile porosity θ_m point to preferential flow. Similarly, long 'cutoff' times t_2 and low mass transfer rates α point to significant tailing and extended residence times of solutes in the soil and aquifer. Analysis of the CTRW and MIM modeling results yields robust interpretations of the subsurface transport regime; increasing our ability to define how solutes interact with, are transported through, and retained within the geologic media. Without incorporating controlling features such as preferential flow, mass transfer, and distinctly high tracer transport velocities into solute transport models we will inaccurately predict solute transport at the SH-CZO and consequently important processes like estimating age of water.

REFERENCES

Adams, E.E., and L.W. Gelhar. 1992. Field study of dispersion in a heterogeneous aquifer: 2. spatial moments analysis. Water Resour. Res. 28:3293-3307.

Al-Jabri, S., R. Horton, D.B. Jaynes , and A. Gaur. 2002. Field determination of soil hydraulic and chemical transport properties 1. Soil Sci. 167:353-368.

Amundson, R., D.D. Richter, G.S. Humphreys, E.G. Jobbagy , and J. Gaillardet. 2007. Coupling between biota and earth materials in the critical zone. Elements 3:327-332, doi: 10.2113/gselements.3.5.327.

Anderson, S.P., R.C. Bales, and C.J. Duffy. 2008. Critical zone observatories: Building a network to advance interdisciplinary study of earth surface processes. Mineral Mag 72:7-10.

Becker, M.W. and A.M. Shapiro. 2003. Interpreting tracer breakthrough tailing from different forced-gradient tracer experiment configurations in fractured bedrock. Water Resour. Res. 39:1024, doi: 10.1029/2001WR001190.

Becker, M.W. and A.M. Shapiro. 2000. Tracer transport in fractured crystalline rock: Evidence of nondiffusive breakthrough tailing. Water Resour. Res. 36:1677-1686, doi: 10.1029/2000WR900080.

Berkowitz, B. and H. Scher. 2009. Exploring the nature of non-Fickian transport in laboratory experiments. Adv. Water Resour. 32:750-755, doi: 10.1016/j.advwatres.2008.05.004.

Berkowitz, B. and H. Scher. 1998. Theory of anomalous chemical transport in random fracture networks. Phys Rev E. 57:5858-5869.

Berkowitz, B., A. Cortis, M. Dentz , and H. Scher. 2006. Modeling non-Fickian transport in geological formations as a continuous time random walk. Rev. Geophys. 44:RG2003, doi: 10.1029/2005RG000178.

Bethke, C.M. and T.M. Johnson. 2008. Groundwater age and groundwater age dating. Annu. Rev. Earth Planet. Sci. 36:121-152.

Bijeljic, B., S. Rubin, H. Scher , and B. Berkowitz. Non-Fickian transport in porous media with bimodal structural heterogeneity. J. Contam. Hydrol. In Press, Corrected Proof:, doi: 10.1016/j.jconhyd.2010.05.007.

Brace,W.F., J.B. Walsh , and W.T. Frangos. 1968. Permeability of granite under high pressure. J. Geophys. Res. 73:2225-2236.

Brantley, S.L., M.B. Goldhaber , and V. Ragnarsdottir. 2007. Crossing disciplines and scales to understand the critical zone. Elements 3:307-314.

Brusseau, M.L., Z. Gerstl, D. Augustijn , and P.S.C. Rao. 1994. Simulating solute transport in an aggregated soil with the dual-porosity model: Measured and optimized parameter values. Journal of Hydrology 163:187-193, doi: 10.1016/0022-1694(94)90028-0.

Brusseau, M.L., R.E. Jessup , and P.S. Rao. 1991. Nonequilibrium sorption of organic chemicals: Elucidation of rate-limiting processes. Environ. Sci. Technol. 25:134-142, doi: 10.1021/es00013a015.

Cameron, D.R., and A. Klute. 1977. Convective-dispersive solute transport with a combined equilibrium and kinetic adsorption model. Water Resour. Res. 13:183-188.

Casey, F.X.M., D.B. Jaynes, R. Horton, and S.D. Logsdon. 1999. Comparing field methods that estimate mobile-immobile model parameters. Soil Sci. Soc. Am. J. 63:800-806.

Coats, K.H., and B.D. Smith. 1964. Dead-end pore volume and dispersion in porous media. Soc. Pet. Eng. J. 4:73-84.

Cortis, A. , and B. Berkowitz. 2004. Anomalous transport in "classical" soil and sand columns. Soil Sci. Soc. Am. J. 68:1539-1548.

Deng, J., X. Jiang, X. Zhang, W. Hu , and J.W. Crawford. 2008. Continuous time random walk model better describes the tailing of atrazine transport in soil. Chemosphere 71:2150-2157, doi: 10.1016/j.chemosphere.2008.01.001.

Dentz, M., H. Scher, D. Holder , and B. Berkowitz. 2008. Transport behavior of coupled continuous-time random walks. Phys Rev E. 78:041110.

Dere, A., T. White, L. Jin, D. Harbor, M. Townsend and S.L. Brantley. 2010. Shale weathering rates across a continental-scale climosequence. *In* Shale weathering rates across a continental-scale climosequence. World congress of soil science, science for a changing world, Brisbane, Austrailia. 1-6 August 2010.

Duffy, C.J. 2010. Dynamical modelling of concentration-age-discharge in watersheds. Hydrol. Process. 24:1711-1718,10.1002/hyp.7691.

Flueckinger, L.A. 1969. Geology of a portion of the Allensville quadrangle, Centre and Huntingdon Counties, Pennsylvania. Rep. 176. Commonwealth of Pennsylvania, State Planning Board, Bureau of Topographic and Geologic Survey.

Gao, G., H. Zhan, S. Feng, G. Huang , and X. Mao. 2009. Comparison of alternative models for simulating anomalous solute transport in a large heterogeneous soil column. J. Hydrol. 377:391-404, doi: 10.1016/j.jhydrol.2009.08.036.

Goltz, M.N. and P.V. Roberts. 1986. Interpreting organic solute transport data from a field experiment using physical nonequilibrium models. J. Contam. Hydrol. 1:77-93, doi: 10.1016/0169-7722(86)90008-2.

Gong, R., C. Lu, W.-. Wu, H. Cheng, B. Gu, D.B. Watson, C.S. Criddle, P.K. Kitanidis, S.C. Brooks, P.M. Jardine , and J. Luo. 2010. Estimating kinetic mass transfer by resting-period measurements in flow-interruption tracer tests. J. Contam. Hydrol. 117:37-45, doi: 10.1016/j.jconhyd.2010.06.003.

Goode, D.J. 1996. Direct simulation of groundwater age. Water Resour. Res. 32:289-296, doi: 10.1029/95WR03401.

Gorelick, S.M., G. Liu , and C. Zheng. 2005. Quantifying mass transfer in permeable media containing conductive dendritic networks. Geophys. Res. Lett. 32: L18402, doi: 10.1029/2005GL023512.

Grisak, G.E., J.A. Pickens , and J.A. Cherry. 1980. Solute transport through fractured media: 2. column study of fractured till. Water Resources Research 16:731-739.

Gwo, J., M.A. Mayes , and P.M. Jardine. 2007. Quantifying the physical and chemical mass transfer processes for the fate and transport of co(II)EDTA in a partially-weathered limestone–shale saprolite. J. Contam. Hydrol. 90:184-202, doi: 10.1016/j.jconhyd.2006.09.013.

Haggerty, R. and S.M. Gorelick. 1995. Multiple-rate mass transfer for modeling diffusion and surface reactions in media with pore-scale heterogeneity. Water Resour. Res. 31:2383-2400.

Haggerty, R. and S.M. Gorelick. 1994. Design of multiple contaminant remediation: Sensitivity to rate-limited mass transfer. Water Resour. Res. 30:435-446.

Hsieh, P.A., and A.M. Shapiro. 1996. Hydraulic characteristics of fractured bedrock underlying the FSE well field at the mirror lake site, grafton county, New Hampshire. *In* Hydraulic characteristics of fractured bedrock underlying the FSE well field at the mirror lake site, grafton county, New Hampshire. U. S. Geological Survey Toxic Substances Hydrology

Program--Proceedings of the technical meeting, Colorado Springs, Colorado. September 20-24, 1993 1996. U. S. Geological Survey Water-Resources Investigations Report 94-4015.

Hsieh, P.A., J.V. Tracy, C.E. Neuzil, J.D. Bredehoeft , and S.E. Silliman. 1981. A transient laboratory method for determining the hydraulic properties of 'tight' rocks—I. theory. Int. J. Rock Mech. Min. Sci. Geomech. Abs. 18:245-252, doi: 10.1016/0148-9062(81)90979-7.

Huang, K., N. Toride , and M.T. van Gencuhten. 1995. Experimental investigation of solute transport in large, homogenous and heterogeneous, saturated soil columns. Transport in Porous Media 18:283-302.

Jardine, P.M., W.E. Sanford, J.P. Gwo, O.C. Reedy, D.S. Hicks, J.S. Riggs , and W.B. Bailey. 1999. Quantifying diffusive mass transfer in fractured shale bedrock. Water Resour. Res. 35:2015-2030, doi: 10.1029/1999WR900043.

Jin, L., R. Ravella, B. Ketchum, P.R. Bierman, P. Heaney, T. White , and S.L. Brantley. 2010. Mineral weathering and elemental transport during hillslope evolution at the Susquehanna/Shale hills critical zone observatory. Geochim. Cosmochim. Acta 74:3669-3691, doi: 10.1016/j.gca.2010.03.036.

Jin, L., G. Rother, D. R. Cole, D. F. R. Mildner, C. J. Duffy, and S. L. Brantley. (2010) Characterization of deep weathering and nanoporosity development in shale – a neutron study. In press for American Minerologist.

Kazemi, G.A., J.H. Lehr, and P. Perrochet. 2006. Groundwater age. John Wiley and Sons, Hoboken, NJ.

Koch, S. and H. Flühler. 1993. Solute transport in aggregated porous media: Comparing model independent and dependent parameter estimation. Water, Air, & Soil Pollution 68:275-289.

Lee, J., R. Horton and D.B. Jaynes. 2000. A time domain reflectometry method to measure immobile water content and mass exchange coefficient. Soil Sci. Soc. Am. J. 64:1911-1917.

Lin, H.S. 2006. Temporal stability of soil moisture spatial pattern and subsurface preferential flow pathways in the shale hills catchment. Vadose Zone J. 5:317-340, doi: 10.2136/vzj2005.0058.

Lin, H.S. and X. Zhou. 2008. Evidence of subsurface preferential flow using soil hydrologic monitoring in the shale hills catchment. Eur. J. Soil Sci. 59:34-49, doi:10.1111/j.1365-2389.2007.00988.x.

Lin, H.S., W. Kogelmann, C. Walker , and M.A. Bruns. 2006. Soil moisture patterns in a forested catchment: A hydropedological perspective. Geoderma 131:345-368, doi: 10.1016/j.geoderma.2005.03.013.

Long, J.C.S., K. Karasaki, A. Davey, J. Peterson, M. Landsfeld, J. Kemeny , and S. Martel. 1991. An inverse approach to the construction of fracture hydrology models conditioned by geophysical data : An example from the validation exercises at the stripa mine. International Journal of Rock Mechanics and Mining Science & Geomechanics Abstracts 28:121-142, doi: 10.1016/0148-9062(91)92162-R.

Luo, J., W.-. Wu, J. Carley, M.N. Fienen, H. Cheng, D. Watson, C.S. Criddle, P.M. Jardine , and P.K. Kitanidis. 2008. Estimating first-order reaction rate coefficient for transport with nonequilibrium linear mass transfer in heterogeneous media. J. Contam. Hydrol. 98:50-60, doi: 10.1016/j.jconhyd.2008.03.002.

Maraqa, M.A., R. B. Wallace , and T. C. Voice. 1997. Effects of degree of water saturation on dispersivity and immobile water in sandy soil columns. J. Contam. Hydrol. 25:199-218, doi: 10.1016/S0169-7722(96)00032-0.

Mayer, A., T. Sandman, and M. Breidenbach. 2008. Effect of flow regime on physical nonequilibrium transport in unsaturated porous media. Vadose Zone J. 7:981-991.

Mayes, M.A., P.M. Jardine, I.L. Larsen, S.C. Brooks , and S.E. Fendorf. 2000. Multispecies transport of metal–EDTA complexes and chromate through undisturbed columns of weathered fractured saprolite. J. Contam. Hydrol. 45:243-265, doi: 10.1016/S0169-7722(00)00108-X.

Neretnieks, I. 1980. Diffusion in the rock matrix: An important factor in radionuclide migration? J. Geophys. Res. 85:4379-4397.

Neuman, S.P. 2005. Trends, prospects and challenges in quantifying flow and transport through fractured rocks. Hydrogeol. J. 13:124-147, doi: 10.1007/s10040-004-0397-2.

Parker, J.C. and A.J. Valocchi. 1986. Constraints on the validity of equilibrium and first-order kinetic transport models in structured soils. Water Resour. Res. 22:399-407, doi: 10.1029/WR022i003p00399.

Perfect, E., M.C. Sukop , and G.R. Hasler. 2002. Prediction of dispersivity for undisturbed soil columns from water retention parameters. Soil Sci. Soc. Am. J. 66:696-701.

Rasmunson, A. and I. Neretnieks. 1986. Radionuclide transport in frast channels in crystalline rock. Water Resour. Res. 22:1247-1256.

Reedy, O.C., P.M. Jardine, G.V. Wilson and H.M. Selim. 1996. Quantifying the diffusive mass transfer of nonreactive solutes in columns of fractured saprolite using flow interruption. Soil Sci. Soc. Am. J. 60:1376-1384.

Reilly, T.E., L.N. Plummer, P.J. Phillips , and E. Busenberg. 1994. The use of simulation and multiple environmental tracers to quantify groundwater flow in a shallow aquifer. Water Resour. Res. 30:421-433, doi: 10.1029/93WR02655.

Renshaw, C.E. 1995. On the relationship between mechanical and hydraulic apertures in rough-walled fractures. J. Geophys. Res. 100:24629-24636, doi: 10.1029/95JB02159.

Seyfried, M.S. and P.S.C. Rao. 1987. Solute transport in undisturbed columns of an aggregated tropical soil: Preferential flow Effects1. Soil Sci. Soc. Am. J. 51:1434-1444.

Silliman, S.E. and E.S. Simpson. 1987. Laboratory evidence of the scale effect in dispersion of solutes in porous media. Water Resour. Res. 23:1667-1673.

Singha, K., F. Day-Lewis , and J.W. Lane J. 2007. Geoelectrical evidence of bicontinuum transport in groundwater. Geophys. Res. Lett. 34:L12401, doi: 10.1029/2007GL030019.

Toride N., F.J. Leij, and M.T. Van Genuchten. 1999. The CXTFIT code for estimating transport parameters from laboratory or field tracer experiments, version 2.1. Rep. 137. U. S. Salinity Laboratory, Agricultural Research Service, U. S. Department of Agriculture, Washington, D.C.

van Genuchten, M.T. and P.J. Wierenga. 1976. Mass transfer studies in sorbing porous media I. analytical solutions. Soil Sci. Soc. Am. J. 40:473-480.

Vanderborght, J., D. Mallants, M. Vanclooster , and J. Feyen. 1997. Parameter uncertainty in the mobile-immobile solute transport model. J. Hydrol. 190:75-101, doi: 10.1016/S0022-1694(96)03064-8.

Vanderborght, J. and H. Vereecken. 2007. Review of dispersivities for transport modeling in soils. Vadose Zone J. 6:29-52, doi: 10.2136/vzj2006.0096.

Varni, M. and J. Carrera. 1998. Simulation of groundwater age distributions. Water Resour. Res. 34:3271-3281, doi: 10.1029/98WR02536.

Appendix A: Soil Properties and Tracer Experiment Data

Appendix A contains soil core retrieval insights, particle size distribution data, soil core photos, modeling details, and some suggested methods for performing soil core tracer experiments.

Soil Core Collection

Intact soil cores were retrieved in three-inch Shelby tubes and a tracked Geoprobe (Figure A1). The numerous rock fragments (Table A1, Figure A1) made it difficult to retrieve intact soil cores from depths deeper than ~60-80 cm without the aid of some hydraulic press such as a Geoprobe. The Geoprobe ran in two modes for retrieval: hydraulic press and hydraulic hammer. Minimal disturbance to the soil is favored; therefore hydraulically pressing the core into the ground is preferred. Due to the many rock fragments, we used a combination of hydraulically pressing the tubes and hammering the tubes. Care was taken to *gently* hammer the tubes with the Geoprobe. At the first indication that the tube was not progressing in the soil, advancement by the Geoprobe ceased and the tube was returned to the surface. Retrieval commenced only after installing a new Shelby tube. To limit jarring of the sample, some researchers will excavate around the Shelby tube prior to removal; we did not do this to minimize disturbance of the field site. Alternative approaches to soil core removal include sculpting a large diameter pedon (15-20 cm) by hand and encasing the soil in wax. The wax-encased sample is then inserted into a large pipe for tracer experimentation. The sculpting method was not used here as the soil was highly cohesive, leading to a good seal between soil and retrieval tube.

Two separate coring holes reaching depths of ~2.6-2.8 m yielded 11 soil cores. Not all recovered soil cores or sections within each core were suitable for tracer test experiments in the laboratory. After removal, samples were capped and stored in a freezer to prevent evaporative cracking and soil structure alteration. Tips for performing successful tracer experiments on intact soil core using Shelby tubes are outlined below.

Soil Core Preparation and Tracer Experiment Methodology

Extreme care must be taken when transporting the soil cores during the preparation phase to prevent artificial development of pathways around the sample. To a perform tracer experiments, one needs a core with nearly flat ends (Figure A1). Identify good sections of the core for the tracer experiments, i.e., target sections of the tube that are not be misshapen or otherwise damaged. The cutting procedure is a step in which the sample is prone to operator destruction. Risks can be minimized by 1) eliminating extensive movement during cutting by securing the core with clamps, and 2) using small amounts of force to cut simultaneously through the aluminum tube and soil. I found that use of a low-speed bandsaw (available at Penn State in the Earth and Mineral Sciences workshop) was most effective as it could simultaneously cut through both rock fragments and soil material (Figure A1). When using the bandsaw, be careful not to vise excessively or secure the sample such that it would deform the shape of the tube; if this occurs the sample could develop by-pass features. Both the cutting rate and the blade speed should be moderately slow to ensure minimum jarring of the sample. Often, the cut will propagate directly and smoothly through shale fragments and soil leaving a flush, even surface. However, a core with an uneven surface as a result of the cutting procedure may be salvageable by filling in void space with an un-reactive aggregate such as quartz sand. Note that if a large amount of aggregate is used between cap and sample calculation of hydraulic conductivity will

change and could change the estimated mass transfer rates. Following cutting of the core, inspect each end for development of by-pass structures.

After cutting, the core is prepared for capping. For the work presented here, schedule 80 chlorinate polyvinyl chloride (CPVC) caps were milled by the EMS workshop to a diameter just greater than the Shelby tube cores. Caps were then partially filled with impermeable epoxy to eliminate dead volume between sample and cap. Sintered frits were ground down to fit in the ends of the caps and secured to the cores using silicone adhesive. Silicone adhesive permits removal and reuse of the caps following the experiments. I found that when the pressure exceeded about 150 kPa (~20 psi) the silicone adhesive failed, and a stronger aluminum-PVC epoxy was needed. Alternatively, one might consider using a permeability cell from Humboldt Construction Material and Testing Equipment to perform hydraulic conductivity and tracer experiments (http://www.humboldtmfg.com/c-2-p-96-id-2.html).

A constant fluid velocity is the ideal condition for tracer experiments. A Cole Parmer Masterflex L/S drive with a six-channel pump head, 7519-15 (Figure A2) was sufficient for soil cores with permeability greater than 10^{-14} m^2, but needed some minor adjustments to pump fluid through soil cores less permeable than this. To generate a larger upstream pressure, we installed larger diameter tubing at the pump head and immediately reduced the tubing size after the pump head (Figure A2). To prevent tubing breakages at the pump head as a result of the increased pressure, we used tubing with a wall thickness of at least 3/16". The reduced tubing size following the pump head should be made of a less pliable material more resistant to expansion, e.g., flexible PVC tubing rather than thin-walled tygon tubing. With regards to tube fittings, single barbed tube fittings are less prone to leakage than multiple barbed fittings. Thin and long zip ties are also useful to prevent leaks.

Prior to injection of tracer, pressure and flow rate should reach a steady-state condition. Reaching steady-state conditions more rapidly can occur by pulling a vacuum on the sample before saturation to eliminate air trapped in pore spaces. In fully saturated media we found that the flow rate will stabilize within a few minutes whereas pressure could take on the order of tens of minutes up to hours depending on the hydraulic diffusivity of the sample. Pressure in initial experiments did not stabilize even after many days; this is thought to reflect the portion of swelling clays in the system (Figure A3). Soil particles will flocculate (structure remains intact) or disperse (clays swell) when low ionic strength solution is applied to them. This phenomenon is readily documented in the in the soil irrigation literature. Predicting flocculation and dispersion is estimated by the sodium adsorption ratio $(SAR) = \dfrac{[Na^+]}{\sqrt{[Ca^{2+}] + [Mg^{2+}]}}$. When SAR is low, we predict flocculation. To keep the SAR low in our soil cores, we use a background solution of 5 mM $CaCl_2$ rather than distilled water, which will promote dispersion in soils. A tracer is then added to the background solution. Large batches of tracer and background solution were mixed prior to injection to prevent changes in background or tracer composition during the experiment. Solutions should be stored in sealable containers to prevent evaporation.

Measurement of tracer effluent generates a concentration history or breakthrough curve (BTC). Measuring the tracer-effluent concentration can be done with ion-specific electrode, ion chromatography, or using a fluid conductivity probe which is a proxy for concentration. Sampling of the effluent by a fraction collector permits equal sample volume at regular time intervals over the course of the experiment. A fraction collector is useful when analyzing the effluent for low concentrations of species such as trace metals, but may not be necessary or more common species at higher concentrations. Note that when concentration boundary conditions

change, a higher frequency of samples should be collected. Common tracer injection periods are greater than three pore volumes. The flow velocities, injection duration, and modeling parameters used in these experiments are listed in Table A2. The effluent concentrations of the bromide and strontium concentrations are listed in Tables A3 and A4.
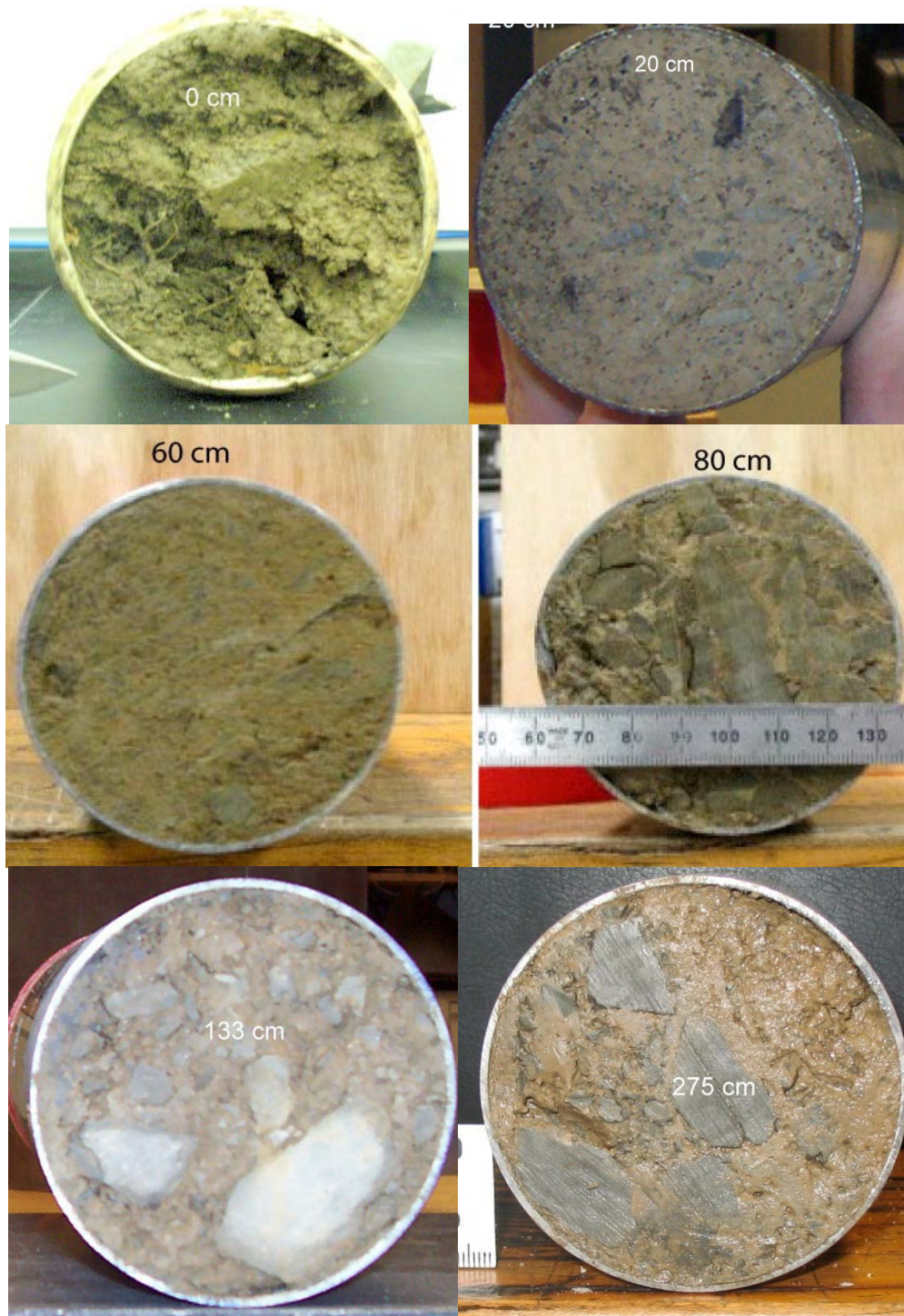
Figure A1. Soil core photos from depths of 0, 20, 60, 80, 133, and 275 cm depths. All soil cores are 7.6 cm (3") in diameter. Frequency and size of shale fragments increase with depth. The 60-80 cm soil core had the largest amount of rock fragments relative to all other soil cores. See Figure 6D and Table A1.

Figure A2. (left) 6 Channel Peristaltic Pump with two installed cartridges, (right) altered tubing configuration for soil cores of lower permeability. Here, separate lines for background solution and tracer solution exist, with a three-way valve to switch between the lines just before the sample. This configuration is prone to changes in flow rate during valve switching but does help eliminate line diffusion. On the right, a larger tubing diameter is installed at the pump head with a reduction in tubing diameter installed immediately after the tubing head; this tubing configuration increases the pressure head. Also note the installed zip ties at the fittings to prevent leakage. Narrow and long zip ties work best.

Figure A3. Physical evidence of swelling clays in the 20-40 cm soil core. During the equilibration period, the swelling of clays actually removed an end cap that was attached with a weak silicone adhesive. The effects of swelling clays was less problematic in the deeper soil cores.

Table A1. Particle Size Distribution Data From Wet Sieving

Depth [m]	[†]total mass [g]	> 6.35 mm [g]	6.35 - 2 mm [g]	2 mm - 63 µm [g]	[††]silt/clay [g]
0.2	149.55	16.99	12.5	36.39	83.67
0.8	388.96	198.99	86.995	50.345	52.63
1.33	180.48	68.79	35.37	28.28	48.04
1.8	322.12	111.7	81.23	78.62	50.57
2.5	476.45	237.71	50.29	30.78	157.67
2.7	278.43	108.08	43.28	45.48	81.59

[†]±0.05 g

[††]silt and clay mass was calculated as the difference between the total mass and the sum of >6.35 mm, 6.35-2 mm, and the 2 mm – 63 µm size fractions.

Table A2. Tracer Experiment Details and Mobile-Immobile Modeling Parameters

[†]Parameter	0-0.2 m	0.6-0.8 m	1.6-1.8 m	2.3-2.5 m	Field
Injection Period [hr]	13.0	10.8	19.5	13.8	2.5
Length [m]	0.194	0.194	0.20	0.20	4.5
EC_{MAX} [mS/cm]	2.40	2.67	2.65	2.57	14.2
EC_{BACK} [mS/cm]	1.13	1.23	1.20	1.19	0.300
q [m/s]	7.64E-06	7.24E-06	3.44E-06	4.30E-06	7.7E-05
			Estimated Parameters		
dispersivity [m]	0.035	0.05	0.05	0.052	0.5
D_{aq} [m^2/s]	2.05E-09	2.05E-09	2.05E-09	2.05E-09	2.05E-09
α [1/s]	1.35E-05	7.80E-06	4.70E-06	1.31E-05	3.50E-06
θ_m [-]	0.18	0.10	0.11	0.14	0.045
θ_{im} [-]	0.26	0.24	0.18	0.15	0.08

[†]EC_{MAX} = maximum fluid conductivity [(mS/cm)/2= kg/m^3], EC_{BACK} = background fluid conductivity, q = specific discharge, D_{aq} = bromide aqueous diffusion coefficient, α = mass transfer rate,

$\theta_{m,im}$ = mobile/immobile porosity

Table A3. Strontium concentrations from soil core tracer tests.

0-0.2 m			0.6-0.8 m			1.6-1.8 m		
time [s]	Sr [ppm]	C/C_o	time [s]	Sr [ppm]	C/C_o	time [s]	Sr [ppm]	C/C_o
0	0.5	0.001[†]	[†]0	0.3	0.001[†]	540	44.9	0.064
1.44E+03	182	0.41	7260	292	0.667	2520	28.9	0.041
8.70E+03	334	0.752	8160	296	0.676	4320	83.2	0.119
4.27E+04	356	0.802	17600	378	0.863	9420	151	0.215
4.67E+04	363	0.818	33300	379	0.865	37740	318	0.453
4.70E+04	367	0.827	38300	390	0.89	69360	353	0.503
5.01E+04	227	0.511	38600	383	0.874	69780	347	0.494
5.37E+04	125	0.282	40900	130	0.297	70560	372	0.53
5.85E+04	89.6	0.202	44200	74.4	0.17	75720	161	0.229
7.75E+04	61.2	0.138	113000	13.8	0.032	83520	94.9	0.135
1.15E+05	29.8	0.067	83800	18.1	0.041	107640	0.3	0
1.67E+05	14.4	0.032	193000	9.9	0.023	135060	28.1	0.04
2.47E+05	6.5	0.015				212160	14	0.02
						297900	8.5	0.012

[†]background concentration

Table A4. Bromide Concentrations from soil core tracer tests.

0-0.2 m			0.6-0.8 m			1.6-1.8 m			2.3-2.5 m		
time [s]	Br [ppm]	C/C_o	time [s]	Br [ppm]	C/C_o	time [s]	Br [ppm]	C/C_o	time [s]	Br [ppm]	C/C_o
0	ND	0	0	ND	0	0	ND	0	0	ND	0
780	91.4	0.113	300	18.1	0.006	540	ND	0	1680	38	0.043
1740	401	0.495	2190	488	0.6	2100	0.5	0	5160	425	0.483
4200	483	0.596	3360	559	0.69	2520	13.7	0.11	8580	555	0.631
10200	672	0.83	4020	533	0.66	4320	44.5	0.35	32580	825	0.938
13530	677	0.836	8160	683	0.84	4740	51.5	0.4	48600	845	0.96
17160	650	0.802	13320	718	0.89	6420	63.9	0.5	53580	575	0.653
17430	698	0.862	14580	773	0.95	9420	77.8	0.61	80760	27	0.031
18300	713	0.88	33300	782	0.97	37800	107	0.84	97440	10	0.011
19200	658	0.812	38340	771	0.95	69420	112	0.88			
31200	754	0.931	38940	756	0.93	69840	109	0.85			
43050	717	0.885	40860	225	0.28	70260	99.4	0.78			
44100	816	1.007	42780	148	0.18	70620	120	0.94	Field Tracer Br		
46740	819	1.011	44160	108	0.13	75780	39.5	0.31	time [s]	Br [ppm]	C/C_o
48300	578	0.713	91260	108	0.016	83580	18.6	0.15	1200	9.4	0.108
49560	437	0.54	101580	94.1	0.014	90900	12.4	0.1	5700	60	0.69
53700	173	0.213				99420	9.06	0.07	7200	70.5	0.81
56700	104	0.129				107700	6.95	0.05	9240	38.1	0.438
58500	117	0.144				114240	5.91	0.05	12000	21.2	0.244
65940	76.1	0.094				120060	4.93	0.04	21600	9.6	0.11
71700	49.8	0.061				131520	3.23	0.03	31800	2.9	0.033
77520	45.5	0.056				132180	3.87	0.03	78600	1.3	0.015
85680	36.2	0.045				135120	3.55	0.03	94800	0.9	0.01
101880	15.1	0.019				143460	3.08	0.02	124800	ND	0
106800	7.1	0.009				156960	2.35	0.02			
110820	10.2	0.013				169800	1.81	0.01			
117900	9	0.011				212220	1.08	0.01			
125220	7.32	0.009				254880	0.67	0.01			
150480	4.32	0.005				297900	0.55	0			
166740	2.82	0.003									

Permeability, Porosimetry, and BET Surface Area Data

We measured the permeability and analyzed the pore space using mercury porosimetry

on the Rose Hill Shale to identify the physical and hydraulic properties limiting fluid flow in

the aquifer at the Shale Hills Critical Zone Observatory (SH-CZO). Understanding the matrix

properties of the shale will help estimate the capacity of the aquifer to store and transmit solutes

over geologic timescales. Figure A4 outlines that geologic media largely composed of shale

and clay tend to have low permeabilities (10^{-23}-10^{-17} m^2) and variable porosity between 0.1 –

0.4 (Neuzil, 1994). As a result, determining the permeability of shale- and clay-rich materials

is challenging, often requiring indirect or unconventional permeability measurements (Brace et

al. 1968; Hsieh et al., 1981).
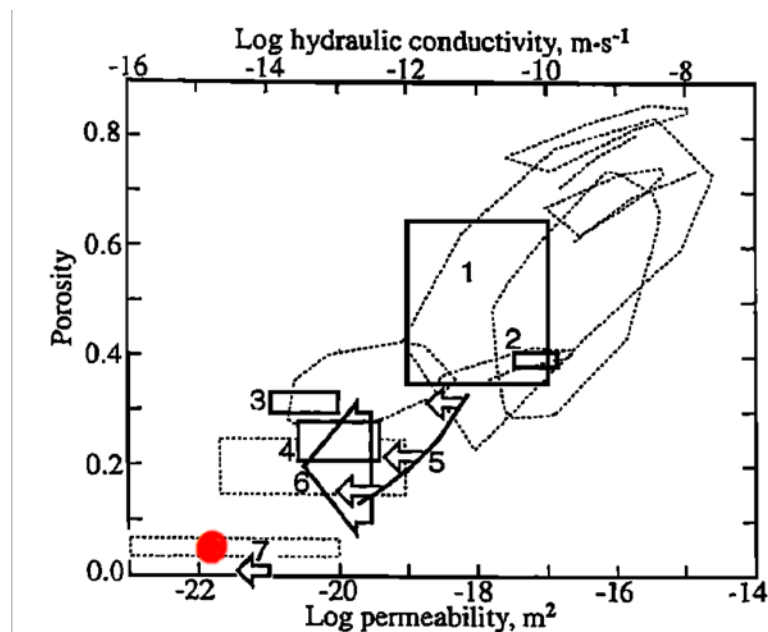
Figure A4. Log-linear relationship between porosity and permeability derived from laboratory
measurements on shale and clay-rich materials. Red dot displays the determined porosity and
permeability from the Rose Hill Shale matrix. (modified from Neuzil, 1994).

We collected numerous samples from a Rose Hill Shale outcrop 3 km southeast of Penn

Roosevelt State Park, Centre County, Pennsylvania (Figure A5). During the coring process

many samples fractured before reaching the experimental length required by the permeability apparatus. Therefore, these results may be biased to more competent sections of the Rose Hill Shale. Note, when coring this shale it was helpful to use a slow bit-speed in addition to water. Vacuum was pulled on the samples for several days and subsequently saturated in deionized water about a week for permeability experiments. Porosimetry measurements only require a few grams of dry shale fragments to perform the analysis. The shale was cored and permeability measured in a triaxial compression apparatus (Figure A6). The entire porosimetry dataset from the Rose Hill Shale is listed in Table A5. Tables A6- B9 contain BET surface area and pore size analysis data on a few soils samples from the SH-CZO and the Rose Hill Shale. Last in this appendix is the Matlab script written by Andy Rathbun used to calculate the permeability on the Rose Hill Shale using pulse-decay method.

Figure A5. Rose Hill Shale cores for measuring permeability and mercury porosimetry. On the left, 3 cores prepared for placement in the triaxial compression apparatus. On the right, the Rose Hill Shale coring samples.
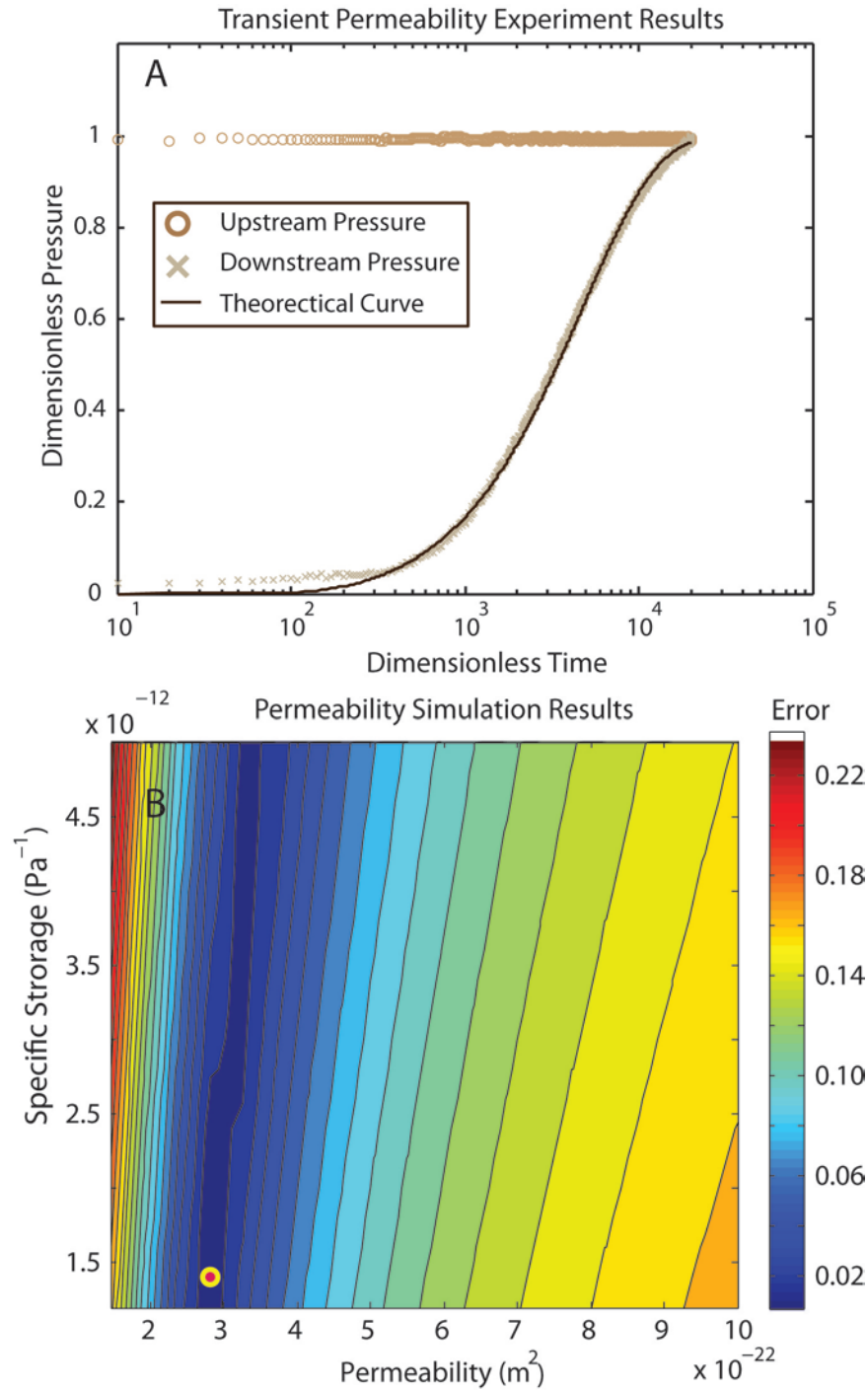
Figure A6. Transient permeability experiment on the consolidated Rose Hill Shale performed in a 30 MPa triaxial compression apparatus. A) Equilibration of the pressure in the downstream reservoir (x's) following a sudden increase of pressure in the upstream reservoir (circles); theoretical permeability curves are fit to the data (solid line), see Hsieh et al. (1981) for the theory and mathematical model. B) Error is minimized at a permeability of 2.8×10^{-22} m^2; however this technique typically results in large errors in specific storage as verified by the

nearly vertical specific storage contours. Neuzil (1994) established a log-linear relationship between porosity and permeability from a large sample of laboratory measurements on shales and clay rich materials. Our calculated permeability of 2.7×10^{-15} m/s $(2.8 \times 10^{-22}$ m$^2)$ coupled with the porosimetry measured porosity of 0.035 plots within the lower limits of porosity-permeability relationship observed by Neuzil (1994), see Figure A4.
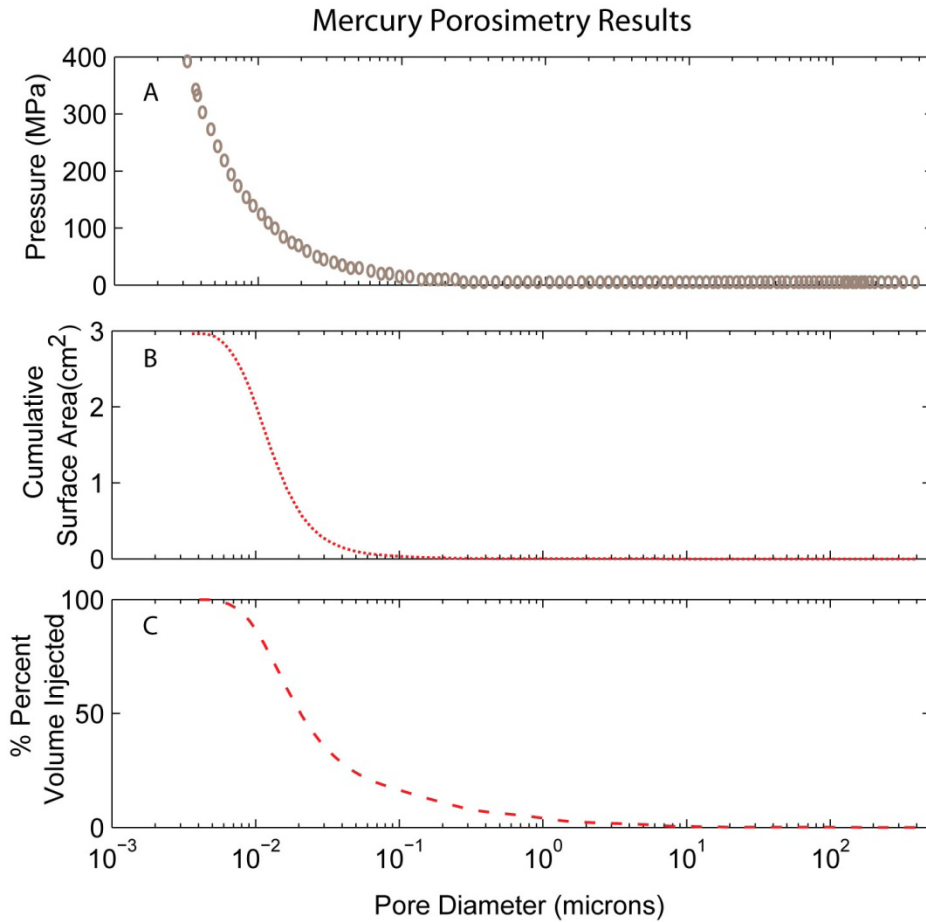
Figure A7. (A) Injection pressure, (B) cumulative surface area, and (C) percent of mercury injected versus pore diameter. The Washburn equation was used to determine pore diameter. Approximately 80% of the pores are less than 0.1 µm. Total porosity can be calculated by

$\theta = \dfrac{V_{Mercury}}{M_{sample}} \cdot \rho_{sample} = \dfrac{0.0138 \text{ cm}^3}{g_{sample}} \cdot \dfrac{2.6 \text{ }g}{\text{cm}^3} = 0.0358 \sim 0.035$. These porosimetry measurements are in

agreement with porosity measurements following water saturation and drying yielding $\sim 3\%$.

Table A5. Mercury Porosimetry Data

Pressure	Pore Diameter	Volume	% of Mercury Injected	dLogP	Area	Cumulative Area
[MPa]	[microns]	[cc/g]	[-]		[mm^2/g]	mm^2
0.003765	390.6429	0	0	0.546	0	0
0.004544	323.4245	0	0	0.6	0	0
0.005212	282.1299	0	0	0.706	0	0
0.005867	250.5971	0	0	0.802	0	0
0.006522	225.5225	0	0	0.897	0	0
0.007164	205.2554	0	0	0.991	0	0
0.007805	188.2873	0	0	1.085	0	0
0.008446	174.093	0	0	1.178	0	0
0.00908	161.8826	0	0	1.27	0	0
0.009722	151.2677	0	0.001	1.363	0	0
0.010349	142.0424	0	0.003	1.455	0	0
0.011128	132.0888	0	0.011	1.557	0	0
0.011893	123.6371	0	0.025	1.669	0	0
0.012824	114.6709	0	0.048	1.791	0	0
0.013776	106.7432	0	0.074	1.927	0	0
0.0149	98.6642	0	0.106	2.078	0	0
0.016079	91.4235	0	0.136	2.245	0	0
0.017361	84.6907	0	0.159	2.423	0	0
0.018912	77.7264	0	0.173	2.628	0	0
0.020553	71.5264	0	0.177	2.86	0	0
0.022436	65.5322	0	0.177	3.115	0	0
0.024345	60.3864	0	0.177	3.39	0	0
0.026538	55.4057	0	0.177	3.686	0	0
0.028999	50.6936	0	0.177	4.023	0	0
0.031709	46.3634	0	0.177	4.398	0	0
0.034688	42.3843	0	0.177	4.81	0	0
0.037907	38.7852	0	0.177	5.259	0	0
0.041617	35.328	0	0.177	5.761	0	0
0.045505	32.3086	0	0.177	6.312	0	0
0.049794	29.5239	0	0.177	6.904	0	0
0.054682	26.8873	0	0.177	7.568	0	0
0.059971	24.5159	0	0.177	8.305	0	0
0.065755	22.3596	0	0.177	9.108	0	0
0.072098	20.3915	0	0.179	9.986	0	0
0.079186	18.5668	0	0.188	10.959	0	0
0.086929	16.9127	0	0.211	12.033	0	0
0.095506	15.394	0	0.256	13.215	0	0
0.105207	13.9743	0	0.312	14.538	0	0
0.117638	12.4976	0.0001	0.367	16.135	0	0
0.131104	11.2139	0.0001	0.403	18.012	0	0
0.145603	10.097	0.0001	0.433	20.039	0	0
0.164274	8.9498	0.0001	0.484	22.431	0	0

Table A5. Mercury Porosimetry Data Continued

Pressure [MPa]	Pore Diameter [microns]	Volume [cc/g]	% of Mercury Injected [-]	dLogP	Area [mm²/g]	Cumulative Area mm²
0.185	7.947	0.0001	0.583	25.284	0	0
0.208842	7.0397	0.0001	0.751	28.509	0.001	0
0.235787	6.2353	0.0001	0.966	32.185	0.001	0.0001
0.266889	5.5086	0.0002	1.174	36.384	0	0.0001
0.299026	4.9166	0.0002	1.316	40.974	0	0.0001
0.334265	4.3983	0.0002	1.423	45.854	0	0.0001
0.379825	3.8707	0.0002	1.542	51.679	0	0.0001
0.437948	3.357	0.0002	1.695	59.154	0	0.0001
0.501125	2.9338	0.0003	1.847	67.946	0	0.0002
0.577877	2.5442	0.0003	1.995	78.049	0	0.0002
0.667061	2.204	0.0003	2.13	90.049	0	0.0002
0.770634	1.9078	0.0003	2.288	103.989	0.001	0.0003
0.931282	1.5787	0.0004	2.601	122.87	0.001	0.0004
1.098066	1.3389	0.0004	3.011	146.668	0.001	0.0005
1.296187	1.1342	0.0005	3.554	173.033	0.001	0.0008
1.54304	0.9528	0.0006	4.218	205.118	0.001	0.0011
1.809426	0.8125	0.0007	4.822	242.348	0.001	0.0015
2.116104	0.6948	0.0007	5.344	283.805	0.001	0.0019
2.485043	0.5916	0.0008	5.795	332.596	0.001	0.0023
3.035086	0.4844	0.0009	6.303	398.321	0.001	0.0028
3.691129	0.3983	0.0009	6.877	485.452	0.001	0.0035
4.295144	0.3423	0.001	7.465	577.497	0.002	0.0044
4.998802	0.2941	0.0011	8.245	672.052	0.002	0.0057
5.77569	0.2545	0.0013	9.18	779.32	0.002	0.0076
6.718803	0.2188	0.0014	10.296	903.501	0.002	0.0102
7.586336	0.1938	0.0015	11.204	1035.483	0.002	0.0127
8.749171	0.168	0.0017	12.231	1181.627	0.002	0.0158
10.00131	0.147	0.0018	13.21	1356.728	0.003	0.0192
11.84799	0.1241	0.002	14.574	1578.816	0.003	0.0248
14.08245	0.1044	0.0022	16.071	1873.451	0.003	0.0321
16.50435	0.0891	0.0024	17.443	2211.155	0.003	0.0399
19.04631	0.0772	0.0026	18.7	2571.494	0.003	0.0483
22.37258	0.0657	0.0028	20.289	2993.949	0.004	0.0606
26.54779	0.0554	0.0031	22.421	3534.705	0.005	0.0801
30.40282	0.0484	0.0034	24.558	4120.521	0.006	0.1029
35.12413	0.0419	0.0038	27.32	4739.589	0.007	0.1367
40.15043	0.0366	0.0042	30.31	5446.643	0.008	0.1788
46.17731	0.0318	0.0047	33.947	6245.115	0.01	0.2376
52.24849	0.0281	0.0052	37.716	7124.136	0.011	0.307
60.40044	0.0243	0.0059	42.923	8147.754	0.013	0.4168
69.59496	0.0211	0.0067	48.857	9403.509	0.015	0.5611
78.39906	0.0188	0.0075	54.501	10713.35	0.016	0.7175
88.92426	0.0165	0.0084	61.035	12110.07	0.017	0.9221
100.8972	0.0146	0.0094	67.888	13738.23	0.017	1.1656
113.7865	0.0129	0.0103	74.388	15540.53	0.016	1.4269
127.8273	0.0115	0.0111	80.417	17491.95	0.015	1.6997

Table A5. Mercury Porosimetry Data Continued

Pressure [MPa]	Pore Diameter [microns]	Volume [cc/g]	% of Mercury Injected [-]	dLogP	Area [mm^2/g]	Cumulative Area mm^2
161.9089	0.0091	0.0125	90.59	22169.29	0.009	2.2467
181.4554	0.0081	0.013	93.968	24860.01	0.007	2.4639
204.2932	0.0072	0.0133	96.421	27924.99	0.005	2.6411
227.5184	0.0065	0.0135	97.954	31269.16	0.003	2.7651
254.6657	0.0058	0.0137	99.043	34911.98	0.002	2.8634
284.5882	0.0052	0.0137	99.665	39045.83	0.001	2.9262
316.9236	0.0046	0.0138	99.933	43557.88	0	2.9564
348.8415	0.0042	0.0138	99.995	48225.01	0	2.9642
359.5737	0.0041	0.0138	99.999	51367.58	0	2.9646
413.7871	0.0036	0.0138	100	55945.28	0	2.9648

Table A6. BET Surface Area from soil and rock samples removed from the Shelby tube soil cores.

depth [m]	Matrix BET Surface Area [m^2/g]	Rock Fragments BET Surface Area [m^2/g]
0.2	11.42	13.22
0.8	14.51	14.53
1.8	12.30	8.32
2.75	9.87	13.61
Rose Hill Shale	12.02	-

Table A7. Summary of surface area data calculated from various methods for the Rose Hill Shale

BET Surface Area	12.02 m^2/g
Langmuir Surface Area	17.46 m^2/g
t-Plot Micropore Area	3.58 m^2/g
t-Plot External Surface Area	8.43 m^2/g
BJH Adsorption cumulative surface area, 17-3000 Å pore diameter	9.76 m^2/g
BJH Desorption cumulative surface area, 17-3000 Å pore diameter	11.59 m^2/g

Table A8. Summary of pore volume data calculated from various methods for the Rose Hill Shale

single point adsorption total pore volume of pores <720 Å @ p/p_0 =0.97	1.97 x 10^{-2} cm^3/g
single point desorption total pore volume of pores <17.7 Å @ p/p_0 =0.14	4.98 x 10^{-3} cm^3/g
t-Plot Micropore Volume	2.02 x 10^{-3} cm^3/g
BJH Adsorption cumulative volume of pores, 17-3000 Å pore diameter	2.48 x 10^{-2} cm^3/g
BJH Desorption cumulative volume of pores, 17-3000 Å pore diameter	2.53 x 10^{-2} cm^3/g

Table A9. Summary of pore Size data for the Rose Hill Shale

BJH Adsorption average pore diameter	101.78 Å
BJH Desorption average pore diameter	87.26 Å

Matlab Script for Calculating Permeability using the Pulse-Decay Method

```
%           Master Code to call the perm calculation code
%                   Written by A. Rathbun Aug 25, 2009
%

%close all
clear all

%Inputs

exp = 'T070-132-133   ';      %For plot naming
sample = 'Shale Hills 1a   ';   %For plot naming
Pc = '3.0 MPa';               %For plot naming

number = 1;                   %Number of stages or experiments preformed, to load

ss=[1.5E-9,2.4E-13]; kk=[1.8E-19,2.3E-22];  %My ranges to investigate
                              %Change these to get better
                              %results, kk = permeability, ss = specific storage
A=0.0253^2*pi; L=.0132;                   %area and length of sample use in experiment [m]
ell=5;      % ell is the divisions between my ranges, 5 for quick looks and
          % setting ranges. 20 for nice finished plots

saver='n'; % y if you want to save the plots

data1 = load('stage2_ND.txt'); % data measured in the triax, non-dimensionalize time and
                              %pressure
%data2 = load('stage3_ND.txt');  Additional measured stages
%data3 = load('stage5_ND.txt');  Additional measured stages

%volume dnstream = 4.23e-7 m^3, dependent on experimental setup
%volume upstream = 6.79e-7 m^3, dependent on experimental setup
%infinite volume = 99e99, dependent on experimental setup

vol1 = [99e99 4.23e-7];   %infinite volume, vol1, vol 2, vol3 are specific to each experiment
vol2 = [6.79e-7 4.23e-7]; %volume upstream
vol3 = [6.79e-7 99e99]; %volume dnstream
comp = 4.47E-10;          %%Compressibility of water
storage1 = vol1/comp;     %[1.0254E-15 4.0830E-16]; % Upstream, Downstream
storage2 = vol2/comp;     % Upstream, Downstream
storage3 = vol3/comp;     % Upstream, Downstream
```

```matlab
%        Calculation portion of the code. Nothing needs be changed

if number == 1
    [perm,spst,tau,Tau,pu,pd] = functry(ss,kk,ell, storage1,A,L,exp,sample,Pc,data1);

    %Plotting permeability, specific storage, and error analysis
    tit = strcat(exp,' ',sample,' ',Pc);
    tit1 = strcat('Perm = ',num2str(perm));
    tit2 = strcat('Storage =',num2str(spst));

    figure
    semilogx(tau,pu(:,1),'b-', 'LineWidth', 2); hold on
    plot(Tau, data1(1:length(data1),2),'bo',Tau,data1(1:length(data1),3),'bx','MarkerSize',6);
    hold on
    semilogx(tau,pd(:,1),'b-', 'LineWidth', 2);
    legend('Theortical','Data')
    xlabel('Dimensionless Time'); ylabel('Dimensionless Pressure')
    title(strvcat(tit,tit1,tit2));


elseif  number == 2
    [perm,spst,tau,Tau,pu,pd] = functry(ss,kk,ell, storage1,A,L,exp,sample,Pc,data1);
    [perm2,spst2,tau2,Tau2,pu2,pd2] = functry(ss,kk,ell, storage2,A,L,exp,sample,Pc,data2);

    Km = (perm+perm2)/2; Ssm =(spst+spst2)/2   %Compute means

    %Plotting Data versus model simulation
    tit = strcat(exp,' ',sample,' ',Pc);
    tit1 = strcat('Perm = ',num2str(perm), 'Perm2 = ',num2str(perm2));
    tit2 = strcat('Storage =',num2str(spst),'Storage2 =',num2str(spst2));

    figure
    semilogx(tau,pu(:,1),'b-', tau2,pu2(:,1),'k-','LineWidth', 2); hold on
    plot(Tau, data1(1:length(data1),2),'bo',Tau2,data2(1:length(data2),2),'ko',...
        Tau, data1(1:length(data1),3),'bx',Tau2,data2(1:length(data2),3),'kx','MarkerSize',6);
    hold on
    semilogx(tau,pd(:,1),'b-',tau2,pd2(:,1),'k-', 'LineWidth', 2);
    legend('Theortical 1','Theortical 2', 'Data1','Data 2')
    xlabel('Dimensionless Time'); ylabel('Dimensionless Pressure')
    title(strvcat(tit,tit1,tit2));

elseif  number == 3
    [perm,spst,tau,Tau,pu,pd] = functry(ss,kk,ell, storage1,A,L,exp,sample,Pc,data1);
    [perm2,spst2,tau2,Tau2,pu2,pd2] = functry(ss,kk,ell, storage2,A,L,exp,sample,Pc,data2);
```

```matlab
    [perm3,spst3,tau3,Tau3,pu3,pd3] = functry(ss,kk,ell, storage2,A,L,exp,sample,Pc,data2);

    Km = (perm+perm2+perm3)/3; Ssm =(spst+spst2+spst3)/3   %Compute means

    %Plotting Permeability
    tit = strcat(exp,' ',sample,' ',Pc);
    tit1 = strcat('Perm = ',num2str(perm), 'Perm2 = ',num2str(perm2),'Perm3 =
',num2str(perm3));
    tit2 = strcat('Storage =',num2str(spst),'Storage2 =',num2str(spst2),'Storage3
=',num2str(spst3));

    figure
    semilogx(tau,pu(:,1),'b-', tau2,pu2(:,1),'k-',tau3,pu3(:,1),'r-','LineWidth', 2); hold on
    plot(Tau, data1(1:length(data1),2),'bo',Tau2,data2(1:length(data2),2),'ko',...
        Tau3, data3(1:length(data3),2),'ro',Tau,data1(1:length(data1),3),'bx',...
        Tau2, data2(1:length(data2),3),'kx',Tau3,data3(1:length(data3),3),'rx','MarkerSize',6);
    hold on
    semilogx(tau,pd(:,1),'b-',tau2,pd2(:,1),'k-', tau3,pd3(:,1),'r-','LineWidth', 2);
    legend('Theortical 1','Theortical 2','Theortical 3','Data1','Data2', 'Data 3')
    xlabel('Dimensionless Time'); ylabel('Dimensionless Pressure')
    title(strvcat(tit,tit1,tit2));
else
    'something is wrong'
end


%%%%Function Called for in Calculation Portion of Code

function P = HYDRO(tau,k, beta,gamma,delta)

    ASYMP=1/(1+beta+gamma); TRANSU=0.0; TRANSD=0.0; SIGMAU=0.0;
SIGMAD=0.0;

    for m=0:10
        phi = BISECT2(m,beta,gamma,delta);
        cs=cos(phi)-delta*phi*sin(phi);
        co=1+beta+gamma-delta*phi^2;
        si=1+gamma+2*delta;
        SIGMAU=cs*exp(-phi^2*tau)/(co*cos(phi)-phi*si*sin(phi));
        SIGMAD=1.0*exp(-phi^2*tau)/(co*cos(phi)-phi*si*sin(phi));
        TRANSU=TRANSU+SIGMAU;
        TRANSD=TRANSD+SIGMAD;
    end
    P(1) = ASYMP+2*TRANSU;
    P(2) = ASYMP+2*TRANSD;
end
```

Appendix B: MIM Parameter Sensitivity

The focus of this appendix is to validate the MIM parameters reported in Table 2 and investigate the range of MIM parameter values for the soil cores that can adequately represent solute transport behavior at the SH-CZO. In Figure B1, I orient the reader on how changes in the MIM parameters, θ_m, θ_{im}, and α change the BTC history for a synthetic example. Note how mobile porosity θ_m shifts the BTC left or right, while immobile porosity controls, in part, the duration of the tailing. The mass transfer rate ALPHA has control on both the peak concentration and the duration of tailing. In Figure B2, I analyze the soil BTCs with the various models, and present the percent error between model data and measured data through time to highlight the goodness of the model fits relative to one another during the various parts of the tracer test.   Finally, I depict the results of hundreds of forward MIM simulations and calculate the RMSE for each simulation to quantify the accuracy of the values reported MIM values in Table 2. I find that the estimated mobile and immobile porosity varies on the order of a 2-3 percent while the mass transfer rate varies on the order of 0.25-0.5/day based on what is considered a "best fit".
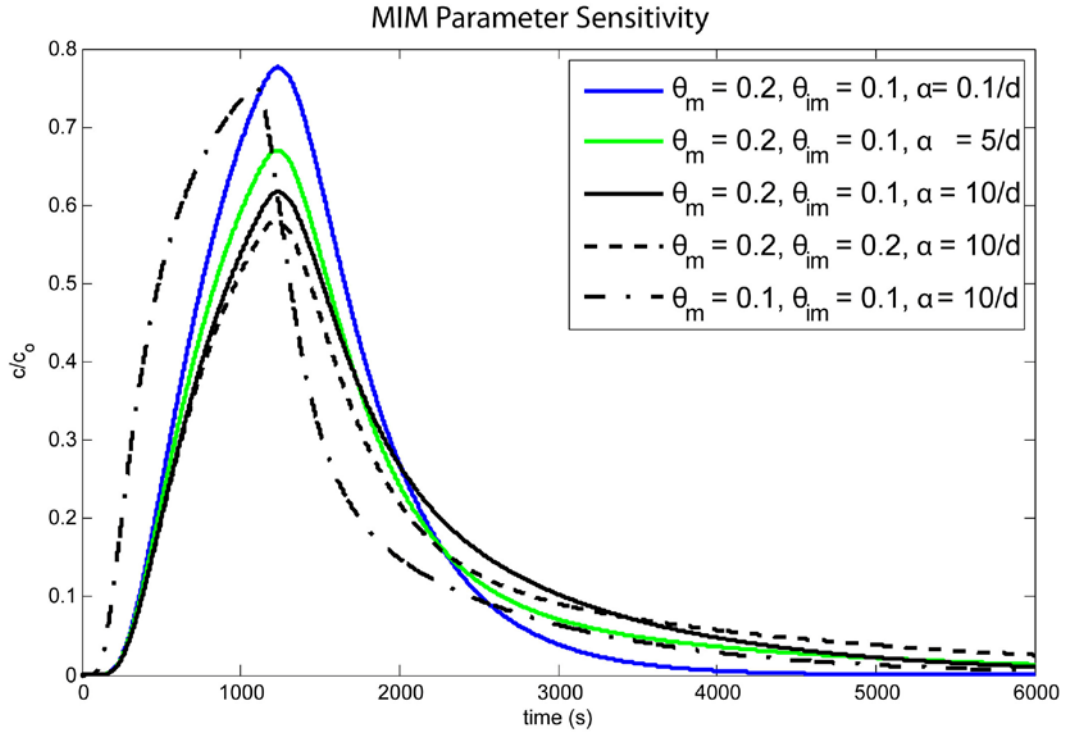
Figure B1. Five similar BTCs to depict MIM parameter sensitivity. Mobile porosity θ_m shifts the entire curve left or right. Immobile porosity controls, in part, the duration of the tailing. The mass transfer rate has control on both the peak concentration and the duration of tailing. For a further analysis concerning the sensitivity and relationship of the MIM parameters see van Genuchten and Wierenga (1976).
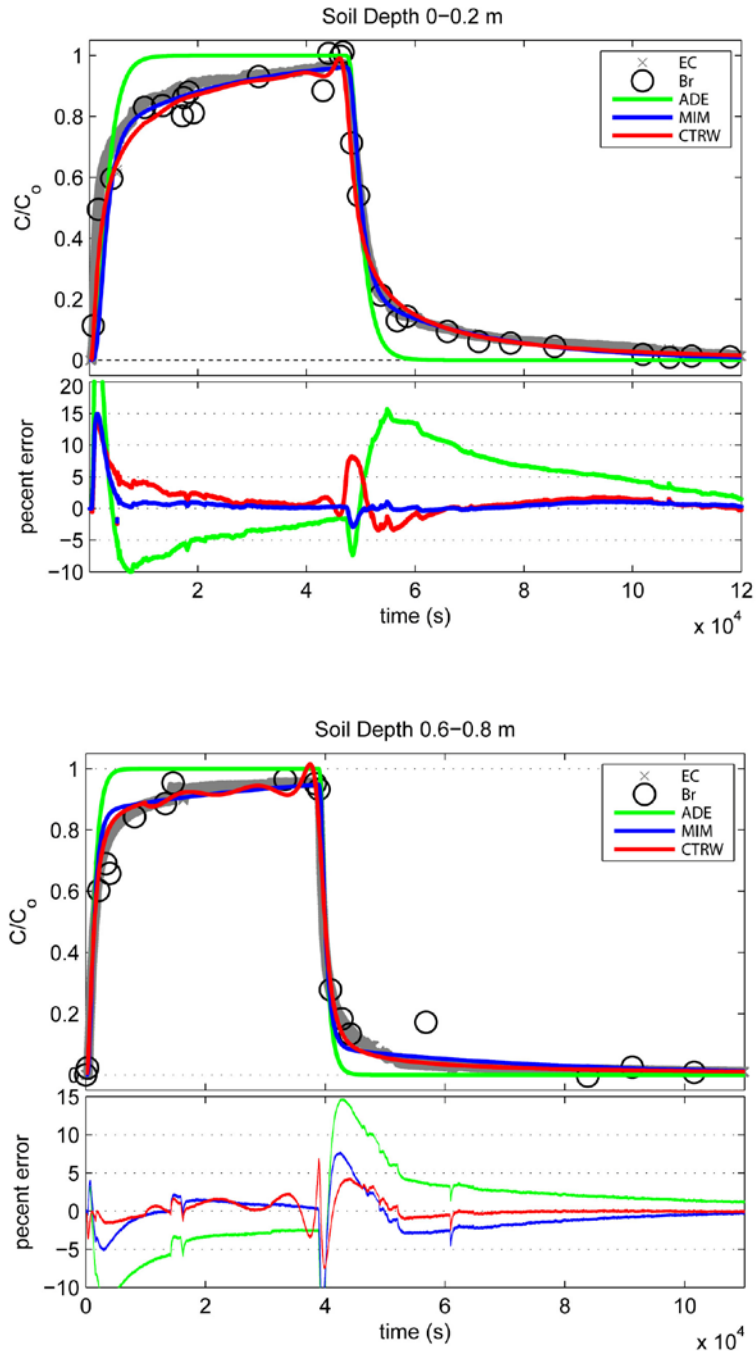
Figure B2. Caption on the following page.
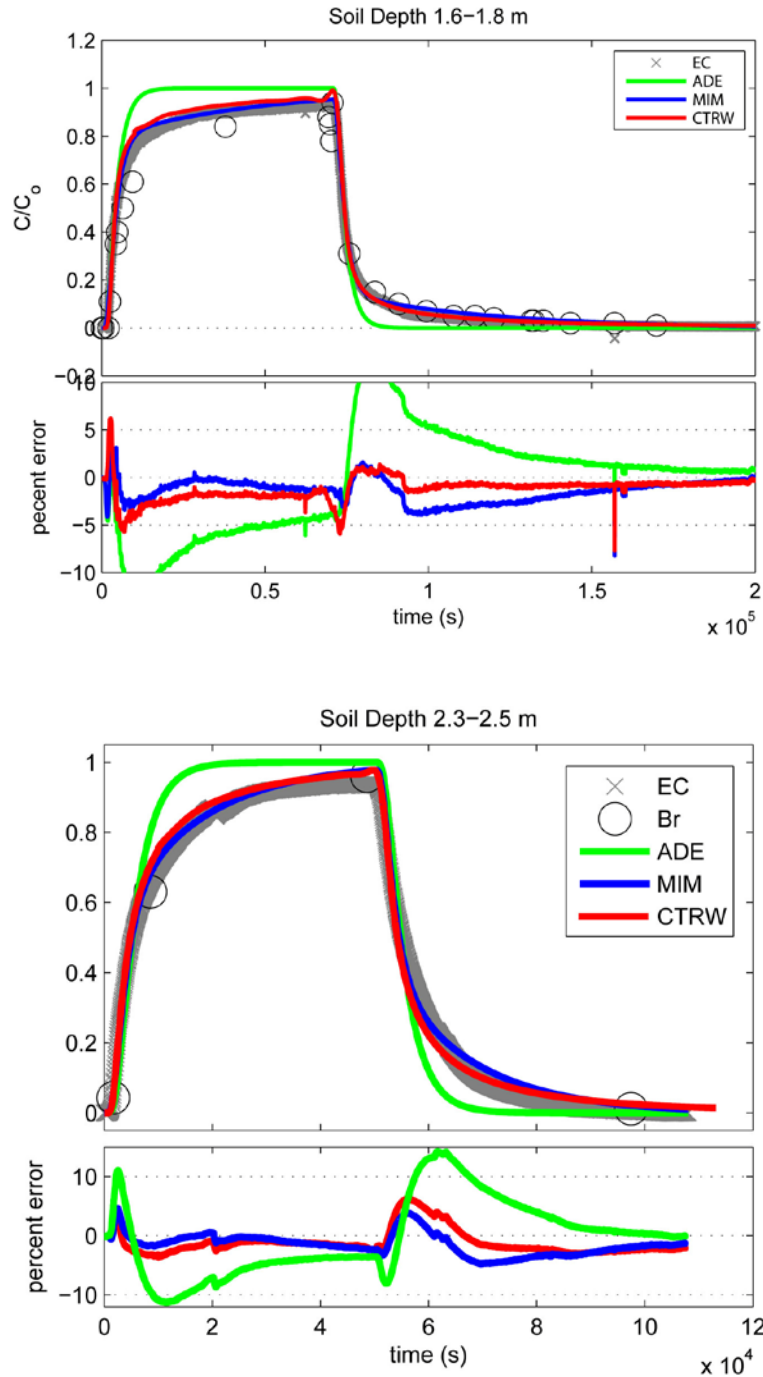
Figure B2. A comparison of model solutions and the measured BTCs using percent error through time. The ADE generally overestimates concentration during injection and underestimates concentration during late times. The MIM and CTRW solutions more accurately represent the entire concentration histories.
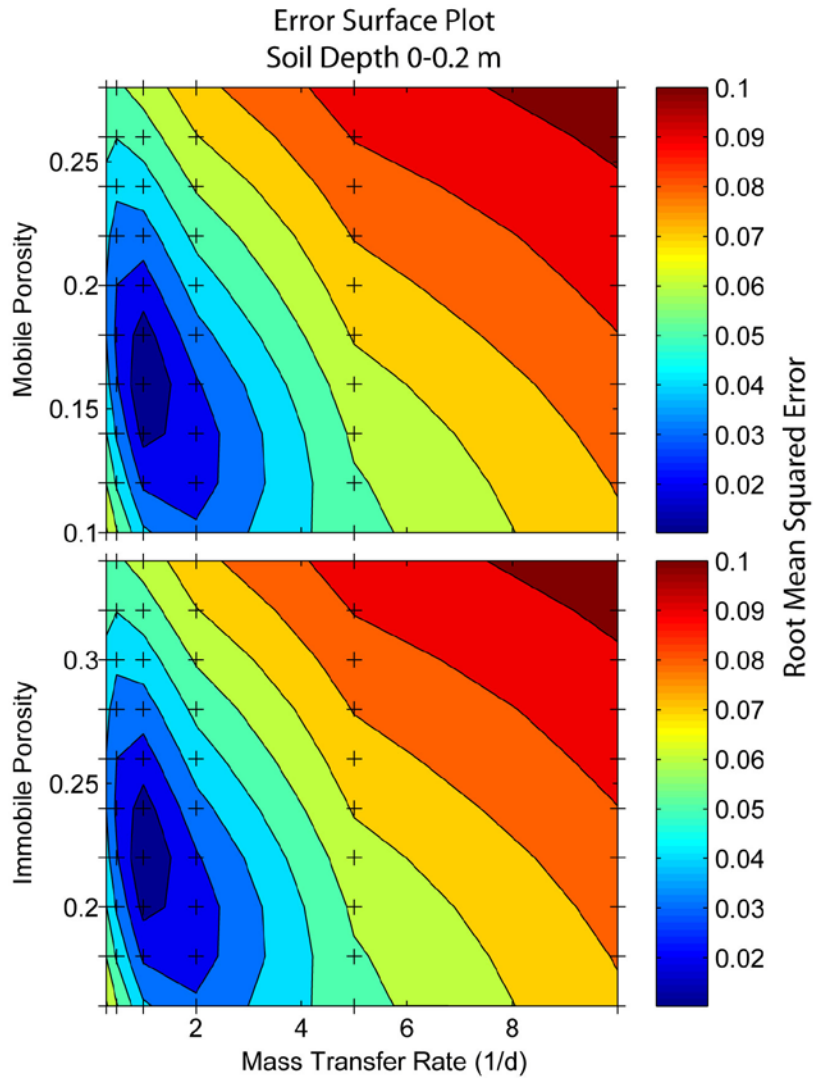
Figure B3. RMSE results from 60 MIM simulations for soil core 0-0.2 m. Crosses represent simulated values. Total measured porosity of this sample is 0.44. Reported best-fit MIM parameters: $\theta_m = 0.18$, $\theta_{im} = 0.26$, $\alpha = 1.17 / \text{d}$.
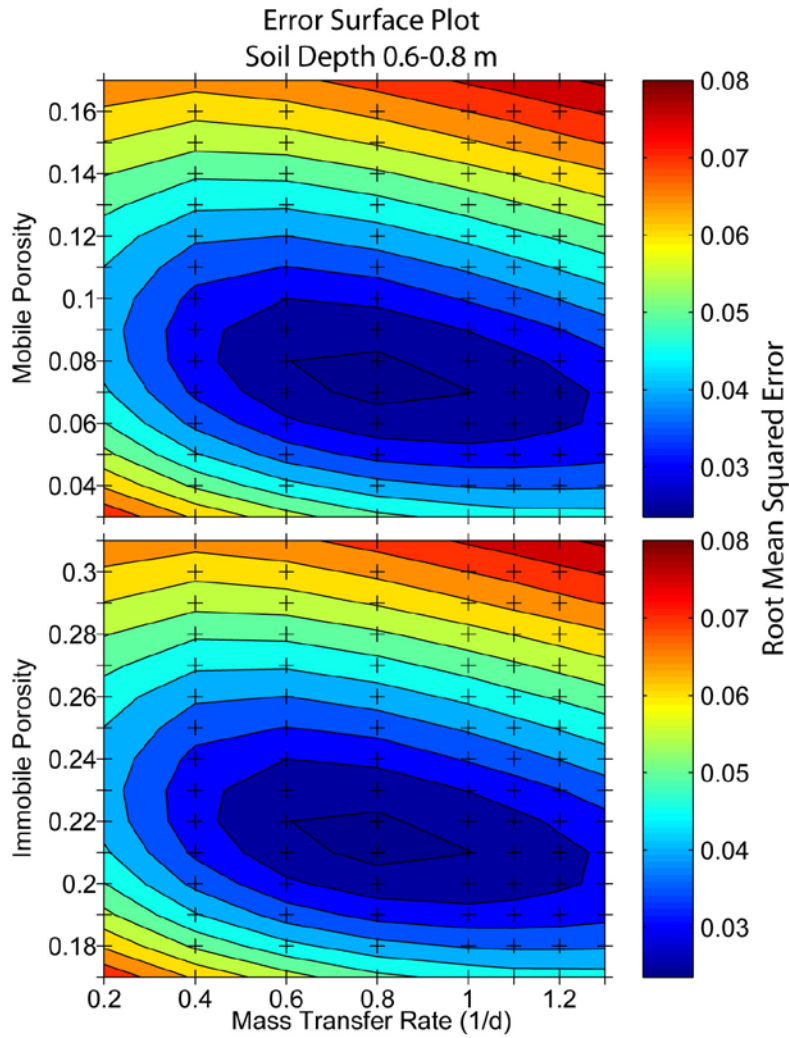
Figure B4. RMSE results from 120 MIM simulations for soil core 0.6-0.8 m.   Crosses represent simulated values. Total measured porosity of this sample is 0.34. Reported best-fit MIM parameters: $\theta_m = 0.10$, $\theta_{im} = 0.23$, $\alpha = 0.67 / d$.
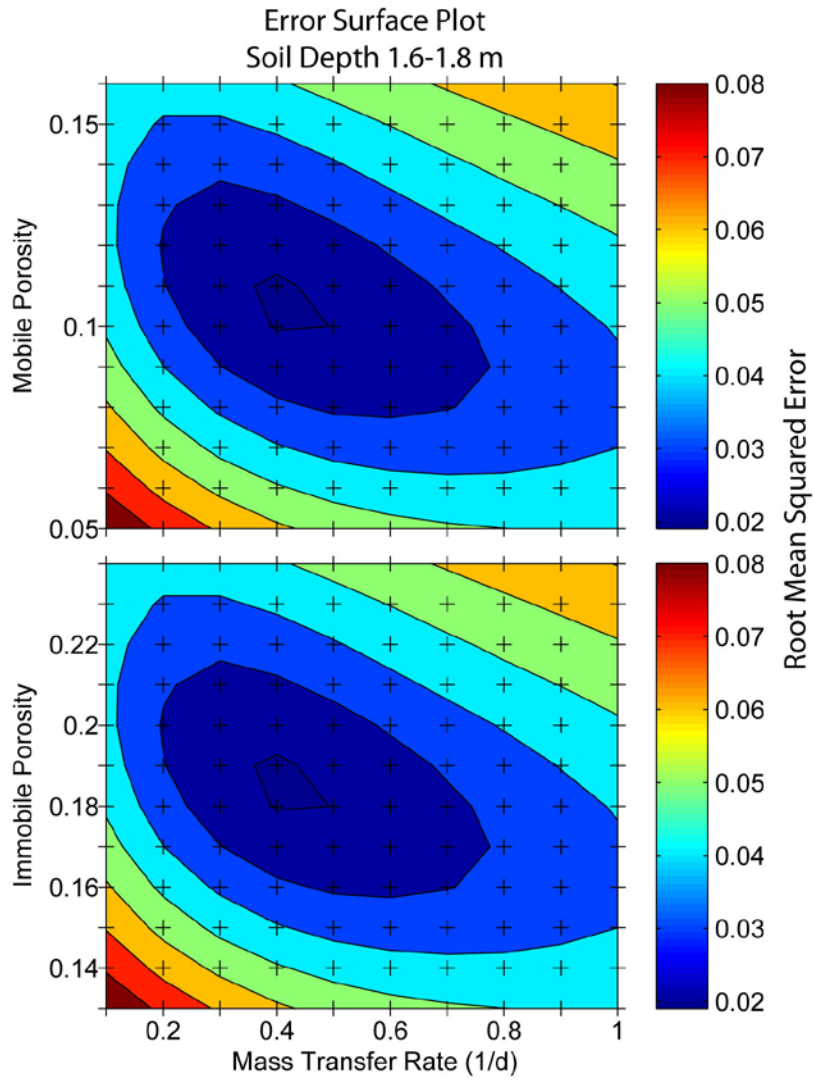
Figure B5. RMSE results from 80 MIM simulations for soil core 1.6-1.8 m. Crosses represent simulated values. Total measured porosity of this sample is 0.29. Reported best-fit MIM parameters: $\theta_m = 0.14$, $\theta_{im} = 0.15$, $\alpha = 1.13/\text{d}$.
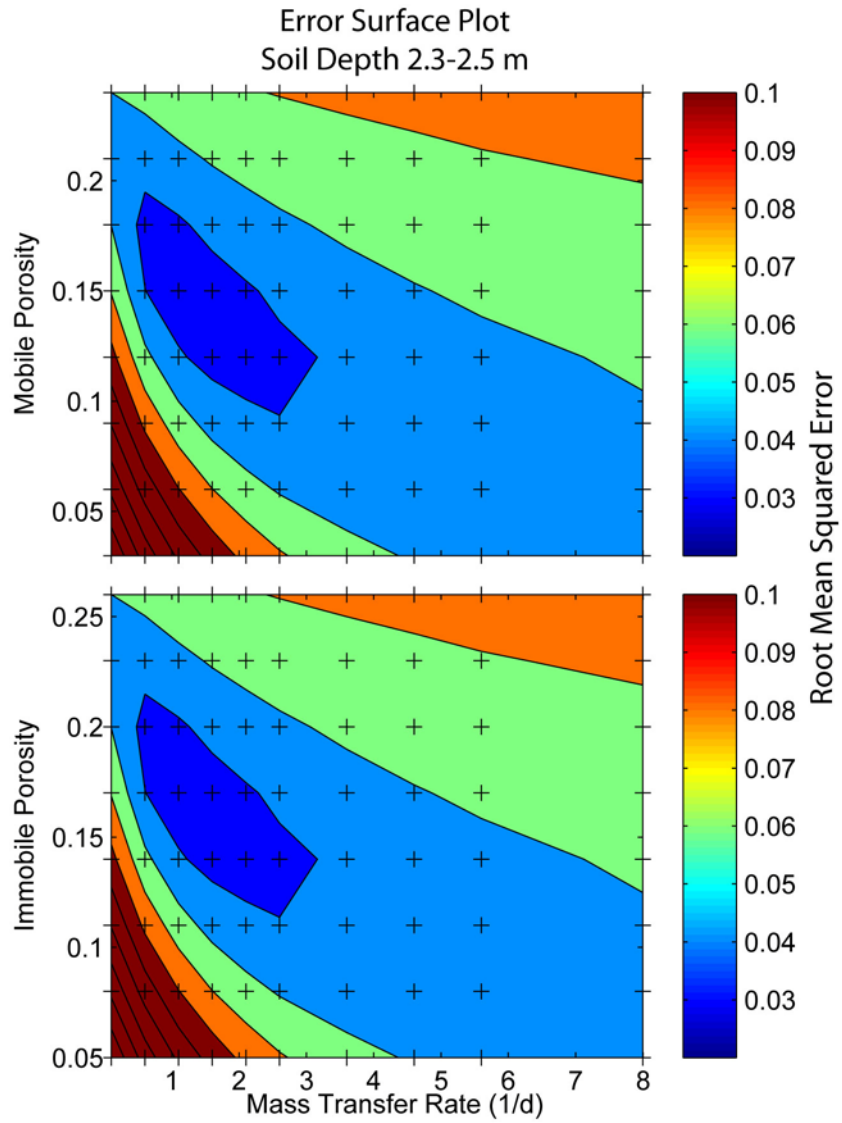
Figure B6. RMSE results from 80 MIM simulations for soil core 2.3- 2.5 m. Crosses represent simulated values. Total measured porosity of this sample is 0.29. Reported best-fit MIM parameters: $\theta_m = 0.14$, $\theta_{im} = 0.15$, $\alpha = 1.13/\text{d}$.

Appendix C: Future Work

These experiments and subsequent modeling results have identified the operation of immobile pore space and mass transfer between mobile and immobile domains on solute transport processes within the SH-CZO's regolith. We identify a range of mass transfer rates for the soil and aquifer at the lab and field scale; these mass transfer rates were based on experiments that continuously inject solute at the inlet boundary and keep the flow velocity steady. An alternative approach to determine mass transfer rates is to use a flow interruption technique. When mass transfer is a contributing process to the overall solute transport behavior, interrupting the test for some period of time during the injection phase at $c/c_\mathrm{o} \approx 0.90$ and again during the elution phase at $c/c_\mathrm{o} \approx 0.10$ often results in a decrease and recovery of the outlet solute concentration after resuming flow (Figure C1).   The decrease and recovery of solute concentration after reinitiating flow is thought to occur due to nonequilibrium concentration between the two fluid domains. Incorporating an interruption in the flow during the tracer test experiment could provide additional constraint on the estimated mass transfer rates. If the estimated mass transfer rate is low, we might underestimate the decrease and recovery concentrations observed in the experiment and the opposite response will occur if the mass transfer rate is too high (Figure C1).

Flow Interruption Experiments
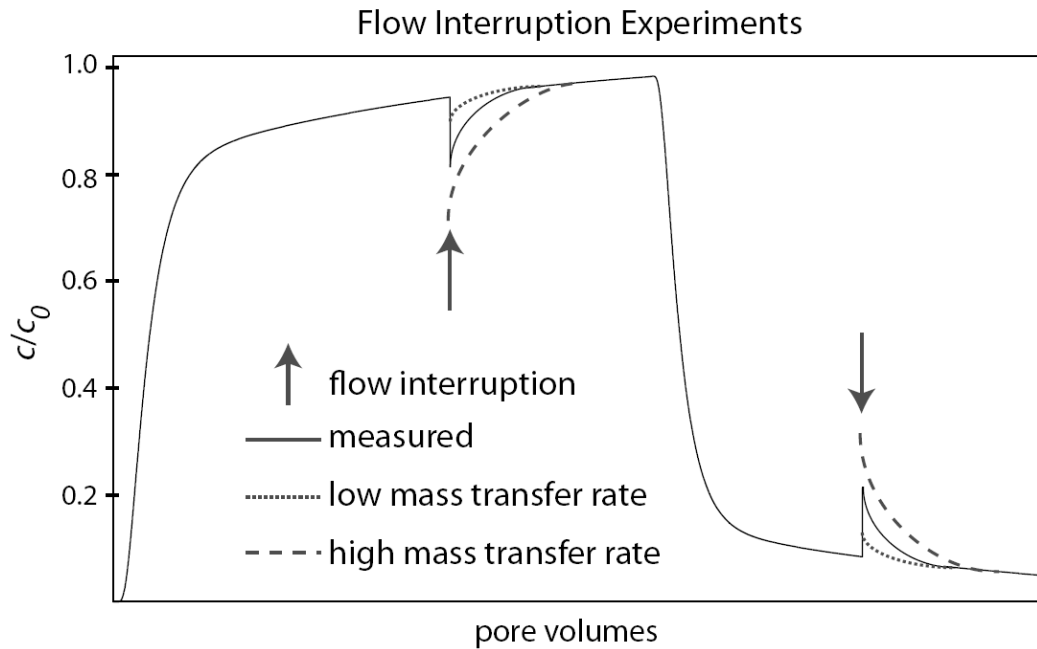
Figure C1. Breakthrough curve showing the effect of flow interruptions during a tracer test. When flow is stopped during the injection phase at $c/c_0 = 0.9$, mass from the mobile domain moves into the immobile domain as a result of nonequilibrium. Reinitiating flow will create a decrease in the measured mobile concentration. If flow is again interrupted during the elution phase of the experiment at $c/c_0 = 0.1$, the measured mobile concentration should increase or rebound. Performing flow interruption experiments provide additional control on the estimated mass transfer rate.

Another consideration for future work would be to analyze our field- and lab-scale concentration data the using other conceptual models than mobile-immobile and CTRW, such as a multi-rate mass transfer (MRMT) model. With MRMT, we could analyze the distribution of mass transfer rates controlling transport behavior in the soil and aquifer.

Redesigning the lab experiments to more closely represent field conditions could be another area of improvement. All the experiments performed in this work occur in fully saturated media to simplify the variables investigated; however, the shallow soils would rarely

become fully saturated. Results from tracer tests performed on unsaturated soil cores may be more representative of field conditions. Similarly, flow in the lower soil profile may not be vertical. Lateral flow is more flow likely deeper into the soil profile. Collecting soil cores oriented parallel to the direction of flow and performing tracer experiments in this orientation may results in an entirely different solute transport behavior.

This thesis focused on the analysis on the physical characteristics of flow and transport using a conservative tracer. A sorbing tracer (strontium) was also employed during these soil core tracer experiments; however we didn't have time to complete the analyses associated with those data. Analysis of this sorbing tracer provides clues to the chemical transport behavior within the soil profile. Understanding the chemical transport behavior of the soil and aquifer permits one to target and identify factors limiting the transport of specific solutes. For example, understanding the transport behavior of specific solutes is important when trying to interpret soil water chemistry with across the catchment.

Reducing the flow velocity and performing tracer experiments that leach tracer through the column experiments could also provide additional insights on the in situ solute transport behavior. Reedy et al. (1996) has shown that when employing a single mass transfer rate between the mobile and immobile domain, the estimated mass transfer rate can be dependent on the flow velocity. Therefore, performing tracer experiments at both high and low flow velocities could identify the range of mass transfer rates occurring in the media. Additionally be performing experiments at long timescales we can more accurately investigate the relationships between weathering and solute transport. The low permeability (2.8 x 10^{-22} m^2) of the unfractured shale bedrock prevented carrying out a tracer experiment in the laboratory. However, performing tracer experiments on a suite of fractured-bedrock samples in the

laboratory would directly examine the extent to which solute transport fractures within the bedrock are controlled by mass transfer.

Besides refinement of lab experiments, additional solute transport experiments at the field scale will help confirm our interpretations of the solute transport behavior at the SH-CZO. Utilizing the existing boreholes to inject a conservative tracer could more accurately quantify the processes and physical properties controlling the residence time of solutes in the subsurface. A field-scale natural-gradient tracer test that is monitored over the course of months to years is more likely to sample a broader spectrum of heterogeneity than encountered in the laboratory.

The methods employed here analyze the mobile fluid domain, while incorporating near-surface geophysical measurements may provide an estimate of the concentration in the immobile domain (Singha et al., 2007). For example, electrical resistivity measurements collected during the field tracer test are yet to be analyzed and incorporated into the tracer transport analysis. Analysis of this electrical resistivity field data will at a minimum depict the location of the solute with respect to time, thus providing better control on the transport behavior observed in the experiment. Similarly, transferring the soil cores from the present aluminum pipe into a PVC pipe would enable electrical resistivity measurements to be conducted in the laboratory.

To test the hypothesis that solutes were retained within shale fragments one could destroy the core sample and attempt to leach bromide and strontium out of the rock fragments. Also, microspheres might be a useful tracer to distinguish between pore diameters that either trap or permit advection of fluid.